IN-CLOUD ICE ACCRETION MODELING ON WIND TURBINE BLADES USING AN EXTENDED MESSINGER MODEL

A Thesis
Presented to
The Academic Faculty

by

Muhammad Ali

In Partial Fulfillment
of the Requirements for the Degree of
Master of Science in the
School of Aerospace Engineering

Georgia Institute of Technology
August 2015

IN-CLOUD ICE ACCRETION MODELING ON WIND TURBINE BLADES USING AN EXTENDED MESSINGER MODEL

Approved by:

Dr. Lakshmi N. Sankar, Advisor
School of Aerospace Engineering
Georgia Institute of Technology

Dr. Daniel P. Schrage
School of Aerospace Engineering
Georgia Institute of Technology

Dr. Jechiel I. Jagoda
School of Aerospace Engineering
Georgia Institute of Technology

Date Approved: April 29, 2015

Dedicated

To the dearest and the nearest ones.

And

To all those who take the least traveled path.

ACKNOWLEDGEMENTS

Sincere thanks to my advisor, Dr. L N Sankar, for his guidance, vision and support through which I have been able to grasp fundamental concepts and gained immense amount of invaluable knowledge, experience and insight. Also, most importantly, for his abundant patience and confidence in me which were key players in completing this study. My heartiest and humble gratitude to the worthy committee members Dr. Schrage and Dr. Jagodda for their valuable time and advice.

Further, I would also like to thank US Department of State and the Fulbright Commission for granting financial assistance for my study program which also extends to my program officers and the staff members at both the Institute of International Education (IIE) and United States Education Foundation in Pakistan (USEFP) who played a vital role in making my dream of graduate studies a reality.

I would also like to express my gratitude and appreciation, though not enough, for all my past and present lab mates, for their all kind of support, encouragement and inspiration. I cannot forget to mention that the basic idea of this study was inspired by the work of my past lab mate, Eliya Wing.

Above all, I am highly touched by the support and love of all my friends, who have been always more than just friends.

TABLE OF CONTENTS

Page

ACKNOWLEDGEMENTS iv

LIST OF TABLES vii

LIST OF FIGURES viii

SUMMARY ix

CHAPTERS

1 INTRODUCTION 1

1.1 Wind Energy in Cold Climate 1
1.2 Research Objectives 2
1.3 Scope of the Study 2

2 PROBLEM DEFINITION AND FORMULATION 3

2.1 Problem Definition 3
2.2 Types of Ice 3
2.3 Problem Formulation 4

3 BLADE ELEMENT MOMENTUM THEORY 6

3.1 Momentum Theory 6
3.2 Blade Element Momentum Theory 6
3.3 Solution Procedure 7
3.4 Tip and Hub Losses 7

4 FLOW FIELD CALCULATIONS 10

4.1 Uniform Flow 10
4.2 Source flow 10
4.3 Vortex flow 11
4.4 Panel Method 11

5 DROPLET TRAJECTORY CALCULATIONS 16

5.1 Assumptions 16
5.2 Equations of Motion 16
5.3 Drag Law 17
5.4 Solution Setup 17
5.5 Time Step Adaptation 18
5.6 Results and Validation 19
5.7 Parametric Analysis 20

6 HEAT TRANSFER COEFFICIENT CALCULATIONS 22
6.1 Transition Prediction 22
6.2 Sutherland's Law 22
6.3 Thwaites' Method 23
6.4 Laminar Heat Transfer Coefficient 23
6.5 Turbulent Heat Transfer Coefficient 23
7 HEAT AND MASS BALANCE 24
7.1 Extended Messinger Model 24
7.1.1 Assumptions 24
7.1.2 Heat Terms 24
7.1.3 Ice Thickness 25
8 VALIDATION 28
8.1 Validation Cases 28
9 CASE STUDIES 30
9.1 Blade Geometry 30
9.2 Airfoil Characteristics 31
9.3 Turbine Performance Predictions 31
9.4 Radial Sections 32
9.5 Test conditions 32
9.6 Radial Distribution of Collection Efficiency 32
9.7 Case I 33
9.7.1 Collection Efficiency 33
9.7.2 Ice Shapes 34
9.7.3 Power Loss 34
9.8 Case II 35
9.8.1 Collection Efficiency 35
9.8.2 Ice Shapes 36
9.8.3 Power Loss 36
9.9 Case III 37
9.9.1 Collection Efficiency 37
9.9.2 Ice Shapes 37
9.9.3 Power Loss 38
10 CONCLUSIONS 41
10.1 Computational Cost 41
10.2 Critical Locations 41
10.3 Sensitivity 42
10.4 Recommendations 42
11
APPENDIX 43
REFERENCES 44

LIST OF TABLES

Page

Table 1: Conditions for validation cases. 28
Table 2: Conditions for cases studies 32
Table 3: Computational cost breakdown. 41
Table 4: Values of constants (air and water properties). 43

LIST OF FIGURES

Page

Figure 1: Schematic of the solution procedure. 5
Figure 2: Local velocity vectors and flow angles 6
Figure 3: Power curves from various approaches 8
Figure 4: Tangential and Normal Forces 9
Figure 5: Normal and tangential force coefficients at 7 m/s. 9
Figure 6: Normal and tangential force coefficients at 10 m/s. 9
Figure 7: Pressure distribution over NACA 0012 15
Figure 8: Adaptive time stepping. 18
Figure 9: Collections efficiency validation. 19
Figure 10: Collections efficiency variations with respect to ambient conditions. 20
Figure 11: Ice shape Case 27 29
Figure 12: Ice shape Case 28 29
Figure 13: Ice shape for Case 29 29
Figure 14: Ice shape for Case 30 29
Figure 15: Ice shape for Case 37 29
Figure 16: Ice shape for Case 38 29
Figure 17: The geometry of the blade. 30
Figure 18: S809 airfoil characteristics. 31
Figure 19: Power curves. 31
Figure 20: Blade radial sections. 32
Figure 21: Distribution of collection along the radius. 33
Figure 22: Collection efficiency for Case I. 33
Figure 23: Ice shapes for sections at 92.5 and 97.5 percent radius. 34
Figure 24: Sectional power loss at 10 m/s wind velocity and 3° pitch angle. 35
Figure 25: Power curve for Case I at 3°pitch angle. 35
Figure 26: Collection efficiency for Case II. 35
Figure 27: Ice shapes for sections at 92.5 and 97.5 percent radius. 36
Figure 28: Sectional power at 10 m/s wind velocity and 3° pitch angle. 36
Figure 29: Power curve for Case II at 3° pitch angle. 36
Figure 30: Sectional collection efficiency at 10 m/s wind velocity and 3° pitch angle. 37
Figure 31: Ice shapes for section 77.5 percent radius. 37
Figure 32: Ice shapes for sections at 82.5, 87.5, 92.5 and 97.5 percent radius. 38
Figure 33: Lift curve for sections at 82.5, 87.5, 92.5 and 97.5 percent radius. 39
Figure 34: Drag curve for sections at 82.5, 87.5, 92.5 and 97.5 percent radius. 39
Figure 35: Sectional power loss at 10 m/s wind velocity and 3° pitch angle. 40
Figure 36: Power curve for Case III at 3° pitch angle. 40

SUMMARY

Wind turbines often operate under cold weather conditions where icing may occur. Icing causes the blade sections to stall prematurely reducing the power production at a given wind speed. The unsteady aerodynamic loads associated with icing can accelerate blade structural fatigue and creates safety concerns.

In this work, the combined blade element-momentum theory is used to compute the air loads on the baseline rotor blades, prior to icing. At each blade section, a Lagrangian particle trajectory model is used to model the water droplet trajectories and their impact on the blade surface. An extended Messinger model is next used to solve the conservation of mass, momentum, and energy equations in the boundary layer over the surface, and to determine ice accretion rate. Finally, the aerodynamic characteristics of the iced blade sections are estimated using XFOIL, which initiate the next iteration step for the computation of air loads via combined blade element theory. The procedure repeats until a desired exposure time is achieved. The performance degradation is then predicted, based on the aerodynamic characteristics of the final iced blades.

The 2-D ice shapes obtained are compared against experimental data at several representative atmospheric conditions with acceptable agreement. The performance of a generic experimental wind turbine rotor exposed to icing climate is simulated to obtain the power loss and identify the critical locations on the blade. The results suggest the outboard of the blade is more prone to ice accumulation causing considerable loss of lift at these sections. Iced formed on the leading edge strongly influences the flow resulting in an early separation over the upper surface. Also, for a tapered and twisted blade, the blades operating at a higher pitch are expected to accumulate more ice. The loss in power ranges from 10% to 50% of the rated power for different pitch settings under the same operating conditions.

CHAPTER 1

INTRODUCTION

Wind Energy in Cold Climate

Wind energy is one of the most promising forms of renewable energy. Wind farms continue to expand around the world. Cold regions and high altitudes offer some of the best locations for wind farms. These locations, however, are innately susceptible to atmospheric icing events during late fall and winter seasons. Cold climate favors accumulation of ice on the wind turbine blade which adversely influences the airfoil aerodynamic characteristics, and decreases the power production. It also causes accelerated structural fatigue of the blades and the gear system, and increases costs associated with turbine maintenance. Ref. 1 states that the "ice accretion represents the most significant threat to the integrity of wind turbines in cold weather." Ice shedding from the blades is also a serious safety concern for nearby communities, roads, power lines etc. Heavy icing prevents continued operation of wind turbines and the disruption may be prolonged in severe conditions. The Swedish statistical incident database reported 161,523 hours of total downtime between 1998-2003, 7% of which were related to cold climate and resulted in 5% or more of production loss [1].

The continued expansion of wind power in regions exposed to icing requires an improved understanding of the relation between icing on wind turbines and the resulting production losses and safety risks. On-site measurements are time consuming, labor intensive, and require long term collection of data for a wind range of ambient conditions. There is a need mathematical and numerical models that complement these field studies, and need to understand and predict icing events. Such simulations are helpful in designing rotors and deicing systems for better performance improved life. An a priori knowledge of ice accumulation and loss of power would also enable power companies to prepare in advance for a steady level of power supply with appropriate backups.

The current models for ice accretion on wind turbines are based on two popular concepts. A commonly used approach for forecasting icing events in wind farms is the model proposed by Makkonen [2], which describes in-cloud icing on a vertically placed, freely rotating cylinder. The ice accretion rate calculated by the model mainly depends on droplet collision efficiency, adhesion efficiency, and accretion efficiency. Icing characteristics on a vertical, freely rotating cylinder are most likely different from icing on a wind turbine blade in circular motion in a vertical plane as the shape, dimensions and air flow are very different. As a result, the Makkonen model can only yield a qualitative estimate of the amount of ice accreted on a given blade surface. A second approach, similar to the approach for aircraft/rotorcraft icing, is based on Computational Fluid Dynamics where aerodynamic parameters are evaluated using commercial CFD solvers followed by ice growth calculations employing numerical codes such as LEWICE, TURBICE or FEN-SAP [3]. These ice growth codes are based on Messinger model. Some of these models have three dimensional capabilities. Since these codes are developed strictly for aviation needs, these analyses include redundant features not applicable to wind turbines. These analyses also ignore some of the important aspects of wind turbines operational environment such as prolonged

exposure to icing conditions and temporal variations in external meteorology. For application on wind turbines, the icing tools must be coupled with numerical weather models and include more of the physics.

Research Objectives

This research work is an effort to better understand the fundamentals of ice accretion on wind turbines and to more reliably predict operational production losses due to icing. Therefore, development of a numerical analysis for ice accretion, validation of the analysis through 2-D and 3-D experimental data, and extraction of knowledge from the validations are the primary research objectives of this study.

Scope of the Study

This research effort begins with a brief survey of wind turbine performance under icing conditions. A physical model called the extended Messinger model is subsequently developed in in MATLAB and validated using available 2-D data. Finally, the applicability to wind turbines is demonstrated by modeling the performance of wind turbines under representative operating conditions, and extracting the distribution of ice shape and mass over the blade surface. This information may then be used in follow-up deicing analyses.

CHAPTER 2

PROBLEM DEFINITION AND FORMULATION

Problem Definition

Prediction of the power losses of a wind turbine under inclement weather conditions requires an understanding of the physics of the problem.

Types of Ice

Depending upon the ambient conditions, ice may form in a variety of ways. These may be roughly classified as in-cloud icing, precipitation icing, and frost. In cloud icing is an ice accretion phenomenon caused by water droplets impinging on a cold surface. It is the subject matter of the present study, and is the most frequently encountered. The resulting ice shape can be further categorized as Rime and Glaze Ice. Glaze ice is the result of liquid precipitation striking surfaces at temperature below the freezing point. Glaze ice is rather transparent, hard and attached firmly to the surfaces. Rime ice occurs when surfaces below the freezing point are exposed to clouds or fog composed of super-cooled water droplets. Its white and opaque appearance is caused by the presence of air bubbles trapped inside the ice. Rime ice is of primary importance in high elevation locations such as hill or mountain tops. Precipitation icing is the freezing of snow or rain after striking a cold surface. Frost is the sublimation of water vapors directly on a cold surface and is common at lower temperatures. However, frost is of low density and strength and therefore does not have significant effects.

The rate of accretion and the amount of ice accumulated on an unheated surface depends on the shape and size of the body, surface roughness, wind speed, ambient temperature and pressure, liquid water content in the air, and the size of the water droplets in the cloud [4]. The process starts with the interception of water droplets by the body. The rate at which the droplets are intercepted is a function of the ability of the body to collect the water droplet, known as the collection efficiency (β), the amount of water present in the cloud or liquid water content (LWC), and the wind speed or free stream velocity (V_∞). The collection efficiency depends on the size and shape of the body (in the present context, the blade chord length c, and the airfoil geometry), effective angle of attack, and the diameter of the droplets. Once the droplets are intercepted, heat transfer occurs from the droplets to the cold surface. Modeling the heat transfer rate requires modeling the kinetic heating, cooling by convection, evaporation or sublimation of the water droplets, and other factors. For freezing to occur, the droplets must lose energy equivalent to the heat of fusion. The heat losses are caused by convection and evaporation. Convective heat transfer depends on the geometry, surface roughness, flow speed, and ambient temperature. The evaporative cooling is a function of the temperature and the pressure at the surface.

If the droplet freezes completely on impact, rime ice is formed. This commonly occurs at low temperatures, low speed, and low LWC. At warm temperatures, high speed and high LWC, not all of the impinging water freezes, but some of its flows down the blade surface. This is known as the run back phenomenon. Warm temperatures and high LWC are conducive to glaze ice formation.

Problem Formulation

The ice accretion may be empirically modeled by an approach proposed by Messinger, and further developed by Myers et al [5]. In this model, the turbine blade is divided into several two-dimensional sections. Ice growth calculations are performed on each section independently. The Messinger model treats the growth of ice as a Stephan phase change problem, which can be described mathematically as,

$$\frac{\partial T}{\partial t} = \frac{k_i}{\rho_i C_{pi}} \frac{\partial^2 T}{\partial y^2}$$

$$\frac{\partial \theta}{\partial t} = \frac{k_w}{\rho_w C_{pw}} \frac{\partial^2 \theta}{\partial y^2}$$

$$\rho_i \frac{\partial B}{\partial t} + \rho_w \frac{\partial h}{\partial t} = \rho_i \beta V_\infty + \dot{m}_{in} - \dot{m}_{e,s}$$

$$\rho_i L_F \frac{\partial B}{\partial t} = k_i \frac{\partial T}{\partial y} - k_w \frac{\partial \theta}{\partial y}$$

Here, T and θ are the temperatures in the ice and water layers, respectively; y is the normal distance measured from the wall; k, ρ and C_p are the thermal conductivity, density and specific heat capacity, respectively; and, the subscripts i and w refer to ice and water respectively. The quantities $\rho_i \beta V_\infty$, $\dot{m}_{in}$ and $\dot{m}_{e,s}$ are the impinging, runback and evaporating (or sublimating) water mass flow rates for a control volume respectively. Finally L_F is the latent heat of solidification of water.

The basic Stephan problem is formulated in terms of the ambient conditions and geometric parameters to give the shape and thickness of ice formed. These parameters include ambient temperature and pressure, liquid water content, wind speed and blade geometry. The solution includes heat and mass balances for each control volume. All possible heat transfers are estimated based on the governing parameters. A Lagrangian based droplet trajectory calculation is employed to determine $\dot{m}_{in}$, the amount of water deposited on the blade surface. Hess-Smith panel method coupled with integral boundary layer approximations gives the necessary flow field parameters.

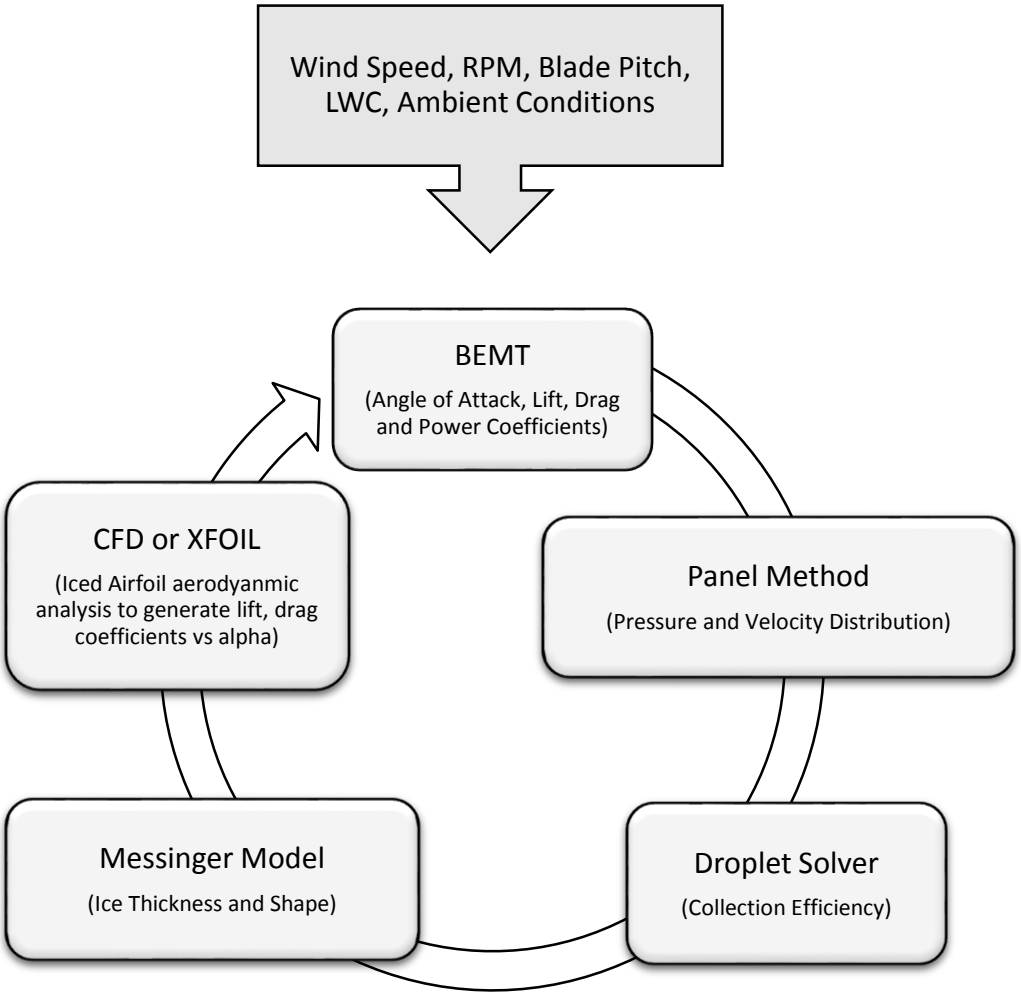

Figure 1: Schematic of the solution procedure.

CHAPTER 3

BLADE ELEMENT MOMENTUM THEORY

Momentum Theory

To evaluate the performance of wind turbines, a basic analysis of momentum transfer is implied. Considering the turbine as a disk across which mass, momentum and energy and conserved and transferred. It is a relatively easy and back-of-the-envelope analysis of turbines.

Blade Element Momentum Theory

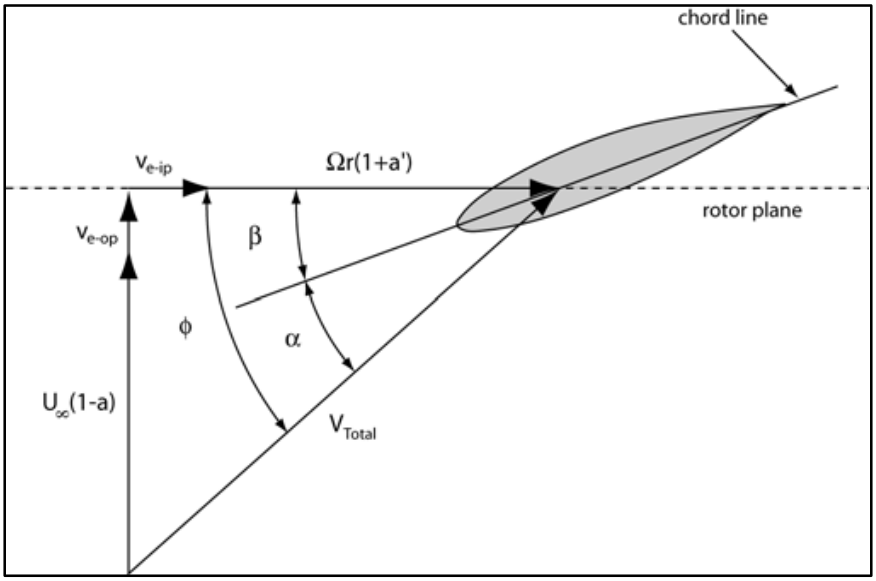

Figure 2: Local velocity vectors and flow angles

Blade element momentum (BEM) theory is one of the oldest and most commonly used methods for calculating induced velocities on wind turbine blades. This theory is an extension of actuator disk theory, first proposed by the pioneering propeller work of Rankine and Froude in the late 19th century. The BEM theory, generally attributed to Betz and Glauert (1935), actually originates from two different theories: blade element theory and momentum theory (Leishman 2000). Blade element theory assumes that blades can be divided into small elements that act independently of surrounding elements and operate aerodynamically as two-dimensional airfoils whose aerodynamic forces can be calculated based on the local flow conditions. These elemental forces are summed along the span of the blade to calculate the total forces and moments exerted on the turbine. The other half of BEM, the momentum theory, assumes that the loss of pressure or momentum in the rotor plane is caused by the work done by the airflow passing through the rotor plane on the blade elements. Using the momentum theory, one can calculate the induced velocities from the momentum lost in the flow in the axial and tangential directions. These induced velocities affect the inflow in the rotor plane and therefore also affect the forces calculated by blade

element theory. This coupling of two theories ties together blade element momentum theory and sets up an iterative process to determine the aerodynamic forces and also the induced velocities near the rotor.

Solution Procedure

The induced velocities, angles of attack and thrust coefficients for each blade element along the span of the blade are determined iteratively. The axial induction factor is estimated as,

$$a = \frac{1}{4}\left[2 + \pi\lambda\sigma - \sqrt{4 - 4\pi\lambda\sigma + \pi\lambda^2\sigma(8\beta + \pi\sigma)}\right]$$

Where $\lambda = \frac{\Omega r}{U_\infty}$ and σ is the rotor solidity. From here, the inflow angle with $a' = 0$, is given by,

$$\tan\varphi = \frac{1 - a}{\lambda(1 - a')}$$

and the sectional thrust coefficient is calculated as,

$$C_T = \frac{\sigma(1 - a)^2(C_l cos\varphi + C_d sin\varphi)}{sin^2\varphi}$$

where φ is the angle of attack, and C_l and C_d are the lift and drag coefficients respectively at that angle of attack. The induction factors are then given by

$$a = \left[1 + \frac{4F sin^2\varphi}{\sigma(C_l cos\varphi + C_d sin\varphi)}\right]^{-1}$$

$$a' = \left[-1 + \frac{4F \sin\varphi \cos\varphi}{\sigma(C_l \sin\varphi - C_d \cos\varphi)}\right]^{-1}$$

Tip and Hub Losses

Since it is assumed there are no hub losses, the loss factor is primarily due to tip losses which is determined by

$$F_{tip} = \frac{2}{\pi} cos^{-1}\, e^{-\left(\frac{B(R-r)}{2rsin\varphi}\right)}$$

$$F_{hub} = \frac{2}{\pi} cos^{-1}\, e^{-\left(\frac{B(R-r)}{2rsin\varphi}\right)}$$

$$F = F_{tip}\, F_{hub}$$

where B is the number of turbine blades and R is the blade radius. The factors a and a' are then recalculated based on the loss factor and the sectional thrust coefficient and then compared to their respective values in the previous iteration.

Once a and a' have converged, the sectional thrust and sectional torque are calculated using

$$dT = 4\pi\rho r U_\infty^2 (1-a) a F dr$$

$$dQ = \frac{1}{2}\rho r V_T^2 (C_l sin\varphi - C_d cos\varphi) \cdot cF dr$$

where U_∞ is the free-stream wind velocity, ρ is the air density, c is the local chord length, and V_T is the total velocity of the incoming air. The sectional thrusts and torques are summed to produce the thrust and torque per blade which are then each multiplied by the number of blades to determine the turbine total thrust and total torque. The turbine's power output is then determined by multiplying the total torque by the blade's angular velocity Ω. The power curve obtained for a 2-bladed wind turbine rotated at a constant speed of 72 RPM and used a linearly tapered, non-linearly twisted S809 airfoil geometry with a 3 degree pitch, is given below in Figure 3. The results presented here are from the work of another graduate student, Greg Harrington.

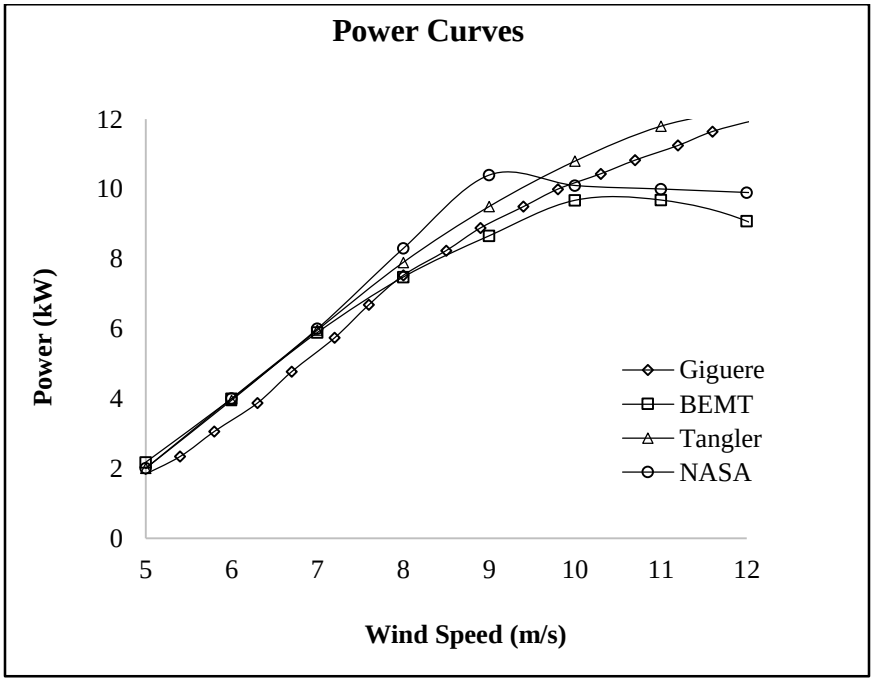

Figure 3: Power curves from various approaches

The normal and tangential force coefficients calculated for equally spaced segments along the blade's length at a wind speed of 7 m/s and 10 m/s are shown in Figure 5 and Figure 6 respectively. A depiction of the normal and tangential forces which are perpendicular and parallel to the airfoil's chord line is provided in Figure and are determined by

$$\alpha = \beta - \varphi$$

$$C_n = C_l \cos(\alpha) + C_d \sin(\alpha)$$

$$C_t = C_l \sin(\alpha) - C_d \cos(\alpha)$$

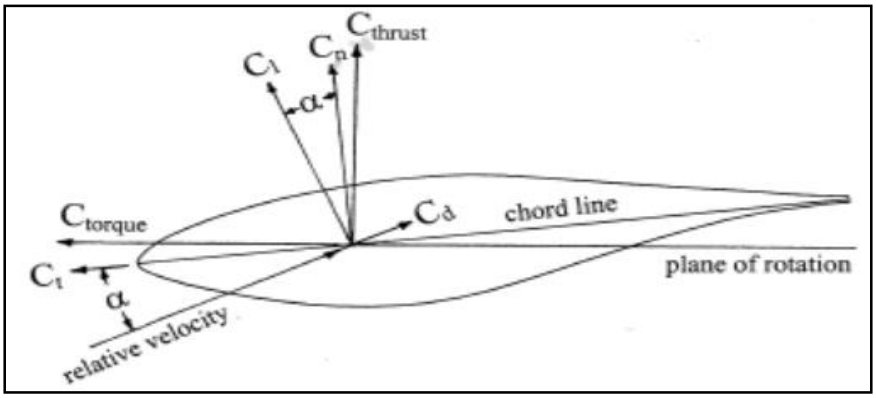

Figure 4: Tangential and Normal Forces

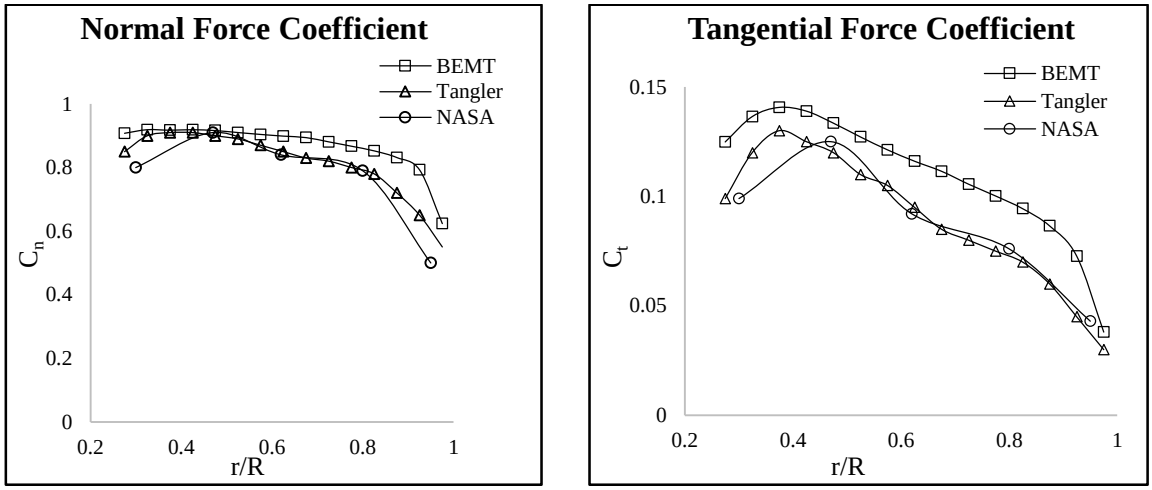

Figure 5: Normal and tangential force coefficients at 7 m/s.

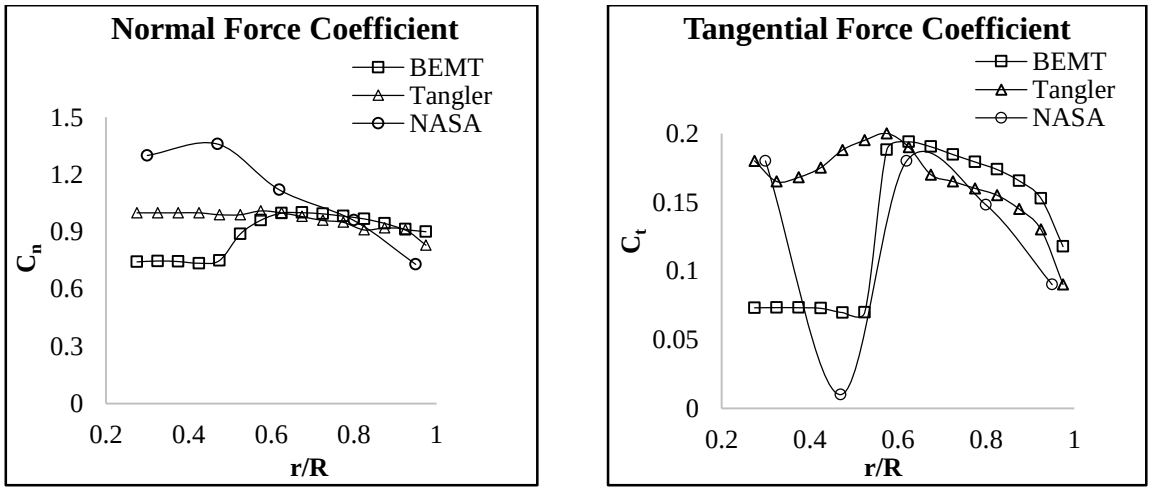

Figure 6: Normal and tangential force coefficients at 10 m/s.

CHAPTER 4

FLOW FIELD CALCULATIONS

In order to proceed, we need information about the flow domain. The velocities at the airfoil surface as well as in the surrounding. The water droplets have to be traced down till the airfoil. The basic way of doing this would be to apply the basic potential theory. Using two dimensional flows and superposition, we can get the resulting flow parameters at a given point.

For the current application, we need the following three potential flows.

Uniform Flow

The free stream flow is modeled as a uniform flow. Uniform flow is a constant velocity flow where the components of velocity remain unchanged.

$$u = A = Constant$$

$$v = B = Constant$$

The potential and stream functions are given by

$$\phi = Ax + By$$

$$\psi = Ay - Bx$$

These satisfy the continuity equation.

Source flow

The velocity field originate form a given fixed point and is symmetric about that point.

$$\frac{v}{u} = \frac{y}{x}$$

The radial velocity from the point of origin at any point at a distance r is given by

$$V = \frac{Q}{2\pi r}$$

$$\phi = \frac{Q}{2\pi} \ln r$$

$$\psi = \frac{Q}{2\pi} \theta$$

Vortex flow

The flow revolves around a given fixed point and is symmetric about that point.

$$\frac{v}{u} = -\frac{y}{x}$$

The radial velocity from the point of origin at any point at a distance r is given by

$$V = \frac{\Gamma}{2\pi r}$$

$$\phi = -\frac{\Gamma}{2\pi}\theta$$

$$\psi = \frac{\Gamma}{2\pi}\ln r$$

Panel Method

Hess-Smith panel method is employed for the calculation of pressure and velocity distributions. This method is based on a vortex and source distribution around an airfoil. The velocity potential ϕ can be expressed as the summation of potentials from the uniform flow ϕ_∞, the sources ϕ_s and the vortex ϕ_v.

$$\phi = \phi_\infty + \phi_s + \phi_v$$

$$\phi_s = \int \frac{q(s)}{2\pi}\ln r \, ds$$

$$\phi_v = -\int \frac{\gamma}{2\pi}\theta \, ds$$

The vortex strength is assumed to be constant over the whole airfoil. The Kutta condition is invoked to fix its value. The source strength is allowed to vary from panel to panel. This source distribution, together with the constant vortex distribution and the free-stream velocity should satisfy the flow tangency boundary condition on the blade surface [6]. The above equation may then be discretized as,

$$\phi = V_\infty(x\cos\alpha + y\sin\alpha) + \sum_{j=1}^{N}\int_{i}^{i+1}\left[\frac{q(s)}{2\pi}\ln r - \frac{\gamma}{2\pi}\theta\right]ds$$

Consider the i^{th} panel to be located between the i^{th} and $(i+1)^{th}$ nodes, with its orientation to the x-axis given by

$$sin\,\theta_i = \frac{y_{i+1} - y_i}{l_i} \qquad \cos\theta_i = \frac{x_{i+1} - x_i}{l_i}$$

where l_i is the length of the panel under consideration.

$$\hat{n}_i \equiv -sin\,\theta_i\,\hat{\imath} + \cos\theta_i\,\hat{\jmath}$$

$$\hat{t}_i \equiv \cos\theta_i\,\hat{\imath} + sin\,\theta_i\hat{\jmath}$$

Furthermore, the coordinates of the midpoint of the panel are given by

$$\bar{x}_i = \frac{x_{i+1} + x_i}{2} \qquad \bar{y}_i = \frac{y_{i+1} + y_i}{2}$$

$$u_i = u(\bar{x}_i, \bar{y}_i)$$

$$v_i = v(\bar{x}_i, \bar{y}_i)$$

The flow tangency condition can be written by setting the normal component as the velocity to zero as,

$$0 = -u_i sin\,\theta_i + v_i \cos\theta_i$$

For the Kutta condition, the tangential velocity at the first and the last point should be equal i.e.

$$u_1 \cos\theta_1 + v_1 sin\,\theta_1 = -(u_N \cos\theta_N + v_N sin\,\theta_N)$$

$$u_i = V_\infty\, cos\,\alpha + \sum_{j=1}^{N} q_i u_{sij} + \gamma \sum_{j=1}^{N} u_{vij}$$

$$v_i = V_\infty\, sin\,\alpha + \sum_{j=1}^{N} q_i v_{sij} + \gamma \sum_{j=1}^{N} v_{vij}$$

where u_{sij}, v_{sij} are the velocity components at the midpoint of panel I induced by a source of unit strength at the midpoint of panel j. A similar interpretation can be found for u_{vij}, v_{vij}. In a coordinate system tangential and normal to the panel, we can perform the integrals in Equation 3 by noticing that the local velocity components can be expanded into absolute ones according to the following transformation:

$$u = u^* \cos\theta_i + v^* \sin\theta_i$$

$$v = u^* \sin\theta_i + v^* \cos\theta_i$$

Now, the local velocity components at the midpoint of the ith panel due to a unit-strength source distribution on this jth panel can be written as

$$u^*_{sij} = \frac{1}{2\pi}\int_0^{l_i} \frac{x^* - t}{(x^* - t)^2 + y^{*2}}\, dt$$

$$v^*_{sij} = \frac{1}{2\pi}\int_0^{l_i} \frac{y^*}{(x^* - t)^2 + y^{*2}}\, dt$$

where (x*, y*) are the coordinates of the midpoint of panel i in the local coordinate system of panel j. Carrying out the integrals in Equation 7 we find that

$$u^*_{sij} = -\frac{1}{2\pi}\ln\left[(x^* - t)^2 + y^{*2}\right]^{\frac{1}{2}}\Big|_{t=0}^{t=l_j}$$

$$v^*_{sij} = \frac{1}{2\pi}\tan\frac{y^*}{x^* - t}\Big|_{t=0}^{t=l_j}$$

These results have a simple geometric interpretation.

$$u^*_{sij} = -\frac{1}{2\pi}\ln\frac{r_{ij+1}}{r_{ij}}$$

$$v^*_{sij} = \frac{v_l - v_0}{2\pi} = \frac{\beta_{ij}}{2\pi}$$

$$\beta_{ij} = atan2\left[\begin{matrix}(\bar{y}_i - y_{j+1})(\bar{x}_i - x_j) - (\bar{x}_i - x_{j+1})(\bar{y}_i - y_j), \\ (\bar{x}_i - x_{j+1})(\bar{x}_i - x_j) + (\bar{y}_i - y_{j+1})(\bar{y}_i - y_j)\end{matrix}\right]$$

$$r_{ij} = \left(x_{ij,q} - \Delta s/2\right)^2 + y^2_{ij,q}$$

Similarly, for the velocity field induced by the vortex on panel j at the midpoint of panel i we can simply see that

$$u^*_{vij} = -\frac{1}{2\pi}\int_0^{l_i} \frac{y^*}{(x^* - t)^2 + y^{*2}}\, dt = \frac{\beta_{ij}}{2\pi}$$

$$v^*_{vij} = -\frac{1}{2\pi}\int_0^{l_i} \frac{x^* - t}{(x^* - t)^2 + y^{*2}}\, dt = \frac{1}{2\pi}\ln\frac{r_{ij+1}}{r_{ij}}$$

$$\sum_{j=1}^{N} A_{ij}\, q_j + \gamma\, A_{iN+1} = b_i$$

$$A_{ij} = -\,u_{sij} \sin\theta_i \;+\; v_{sij} \cos\theta_i$$

$$= -\,u^*_{sij}\left(\cos\theta_j \sin\theta_i \;-\sin\theta_j \cos\theta_i\right) \;+\; v^*_{sij}\left(\sin\theta_j \sin\theta_i \;+\cos\theta_j \cos\theta_i\right)$$

$$2\pi\, A_{ij} = \sin\left(\theta_i - \theta_j\right)\, \ln\frac{r_{ij+1}}{r_{ij}} + \cos\left(\theta_i - \theta_j\right)\beta_{ij}$$

For the vortex strength coefficient

$$2\pi\, A_{iN+1} = \cos\left(\theta_i - \theta_j\right)\, \ln\frac{r_{ij+1}}{r_{ij}} - \sin\left(\theta_i - \theta_j\right)\beta_{ij}$$

The right hand side of this matrix equation is given by

$$b_i \;=\; V_\infty \sin(\theta_i - \alpha)$$

We get an additional one provided by the Kutta condition.

$$\sum_{j=1}^{N} A_{N+1j}\, q_j + \gamma\, A_{N+1,N+1} = b_{N+1}$$

After some manipulations we get

$$2\,\pi\, A_{N+1,j} \;=\; \sum_{k=1,N} \sin(\theta_k - \theta_j)\beta_{kj} - cos\,\left(\theta_k - \theta_j\right) \ln\frac{r_{kj+1}}{r_{kj}}$$

$$2\,\pi\, A_{N+1,N+1} \;=\; \sum_{k=1,N}\sum_{j=1}^{N} \sin\left(\theta_k - \theta_j\right) \ln\frac{r_{kj+1}}{r_{kj}} - cos\,\left(\theta_k - \theta_j\right)\beta_{kj}$$

$$b_{N+1} \;= -V_\infty \cos(\theta_1 - \alpha) - V_\infty \cos(\theta_N - \alpha)$$

where the matrix A is of size (N + 1) × (N + 1). This system can be sketched as follows:

$$\begin{bmatrix} A_{1,1} & \dots & A_{1,j} & \dots & A_{1,N} & A_{1,N+1} \\ \vdots & & \vdots & & \vdots & \vdots \\ A_{i,1} & \dots & A_{i,j} & \dots & A_{i,N} & A_{i,N+1} \\ \vdots & & \vdots & & \vdots & \vdots \\ A_{N,1} & \dots & A_{N,j} & \dots & A_{N,N} & A_{N,N+1} \\ A_{N+1,1} & \dots & A_{N+1,j} & \dots & A_{N+1,N} & A_{N+1,N+1} \end{bmatrix} \begin{bmatrix} q_1 \\ \vdots \\ q_j \\ \vdots \\ q_N \\ q_{N+1} \end{bmatrix} = \begin{bmatrix} b_1 \\ \vdots \\ b_i \\ \vdots \\ b_N \\ b_{N+1} \end{bmatrix}$$

These various expressions set up a matrix problem of the kind $Ax = b$ which can be solved easily in MATLAB.

This equation may be solved numerically for the unknown source strength *q(s)*. We subsequently obtain the pressure and velocity distribution on the airfoil surface. Pressure distribution over NACA 0012 airfoil obtained for two angles of attack is shown below in Figure 7. The results are in reasonable agreement with an inviscid XFOIL data.

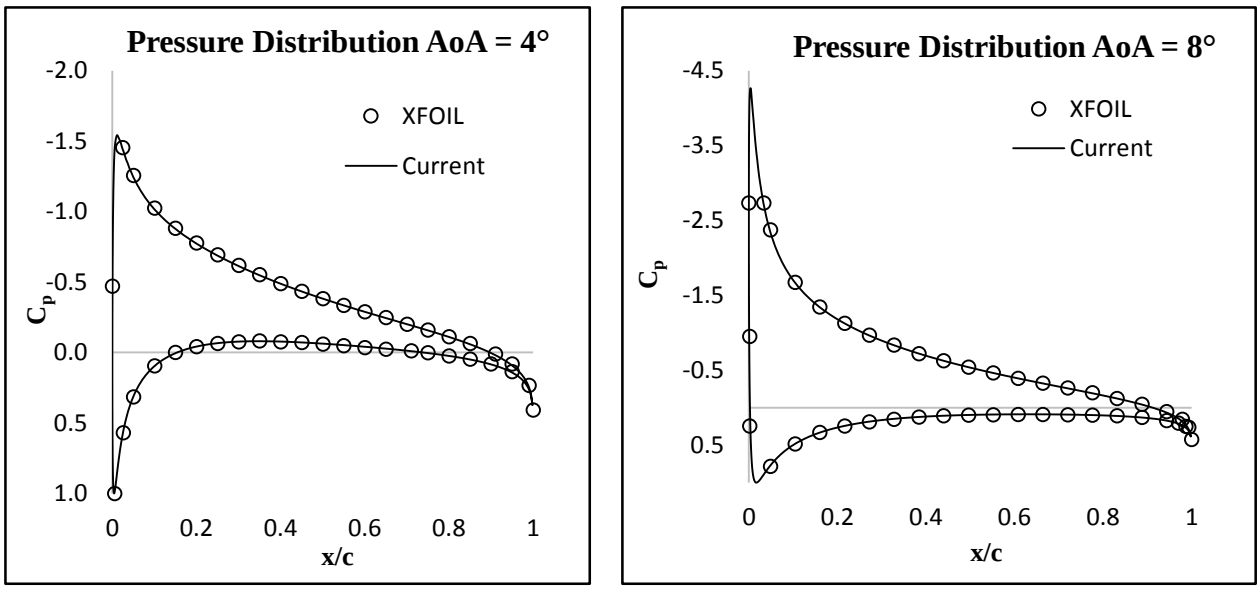

Figure 7: Pressure distribution over NACA 0012

To map this solution to the flow domain, similar approach can be applied [7].

CHAPTER 5

DROPLET TRAJECTORY CALCULATIONS

Assumptions

1. The droplets are spherical and remain spherical.
2. The flow field is undisturbed because of the presence of the particles.
3. The particle motion is dictated only by the aerodynamic drag force and the gravitational pull.

Equations of Motion

Considering motion in two dimensions, Newton's second law states that,

$$m\ddot{x}_p = \sum F_x$$

and

$$m\ddot{y}_p = \sum F_y$$

The only force in the x-direction that we are considering is the component of drag in x-direction while in y-direction, the drag component is accompanied by the gravitational force. Thus, the equations of motion becomes, which are solved for the entire flow field to get the droplet trajectories.

$$m\ddot{x}_p = -D\ cos\,\gamma \qquad m\ddot{y}_p = -D\ sin\,\gamma + mg$$

where

$$\gamma = tan^{-1}\frac{\dot{y}_p - V_y}{\dot{x}_p - V_x} \qquad D = \frac{1}{2}\rho V^2 C_D A_p \qquad V = \sqrt{\left(\dot{x}_p - V_x\right)^2 + \left(\dot{y}_p - V_y\right)^2}$$

Drag Law

The drag coefficient for the droplets are determined by the following drag law.

$$C_D = \begin{cases} 1 + 0.197Re^{0.63} + 2.6 \times 10^{-4} Re^{1.38}, & x \leq 3500 \\ (1.699 \times 10^{-5}) Re^{1.92}, & x > 3500 \end{cases}$$

where $Re = \frac{\rho V d_p}{\mu}$ is the Reynolds Number based on the droplet diameter d_p, the relative velocity V and air viscosity μ. Finally, the collections efficiency is given by the ratio of distance between two water droplets at the release plane and at the impact location.

Solution Setup

The equation of motion is treated is a set of differential equations for the velocity of the particle at a given point which then can be solved by a time-marching approach.

$$\frac{d}{dt}(\dot{x}_p) = -\frac{D}{m}\cos\gamma$$

$$\frac{d}{dt}(\dot{y}_p) = -\frac{D}{m}\sin\gamma + \mathrm{g}$$

The above set of equations are ordinary differential equations which can be solved by a time-stepping Runge-Kutta fourth order numerical scheme.

$$\beta = \frac{dy_0}{ds}$$

Time Step Adaptation

The solution is very sensitive to the time step. So, an adaptive time step is define that adjusts itself as the particle approaches the body. The time step gets finer as it comes closer to the body. The quarter chord of the airfoil is taken as the reference point where the time step is minimum. The time step is define similar to an error function as,

$$\Delta t = 10^{-4}\left(1 - e^{-(\frac{x}{c} - 0.25)}\right)$$

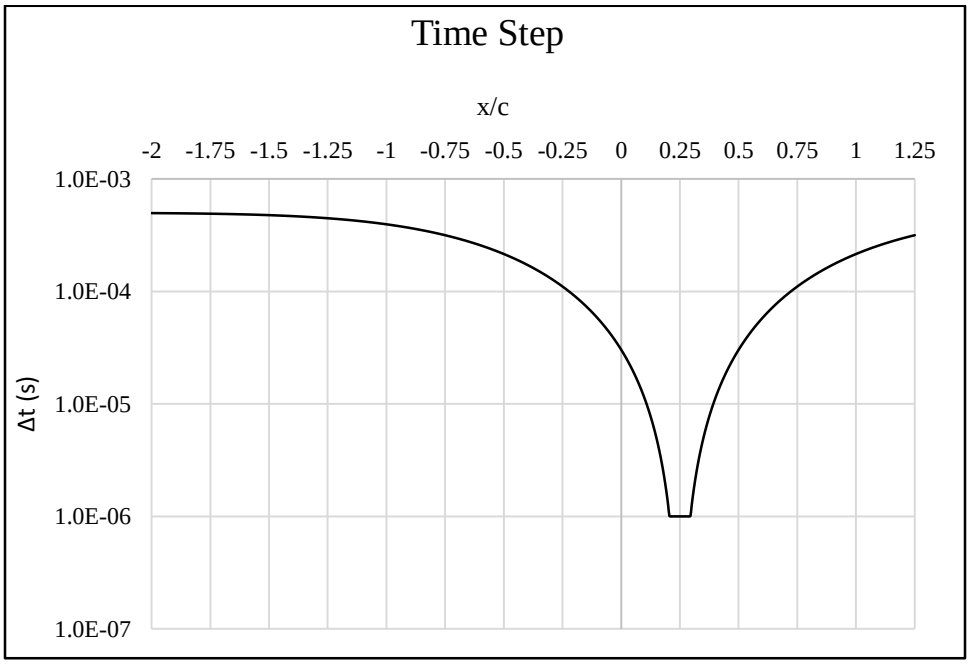

Figure 8: Adaptive time stepping.

Results and Validation

The data generated is compared with the data from Kim et al [8], shown in Figure 9 in which the collection efficiency is plotted against the curvilinear distance over the surface of the airfoil, staring from the stagnation point. The negative x-axis corresponds to the lower surface whereas the positive x-axis corresponds to the upper surface. Acceptable agreement is found between the collection efficiency distributions.

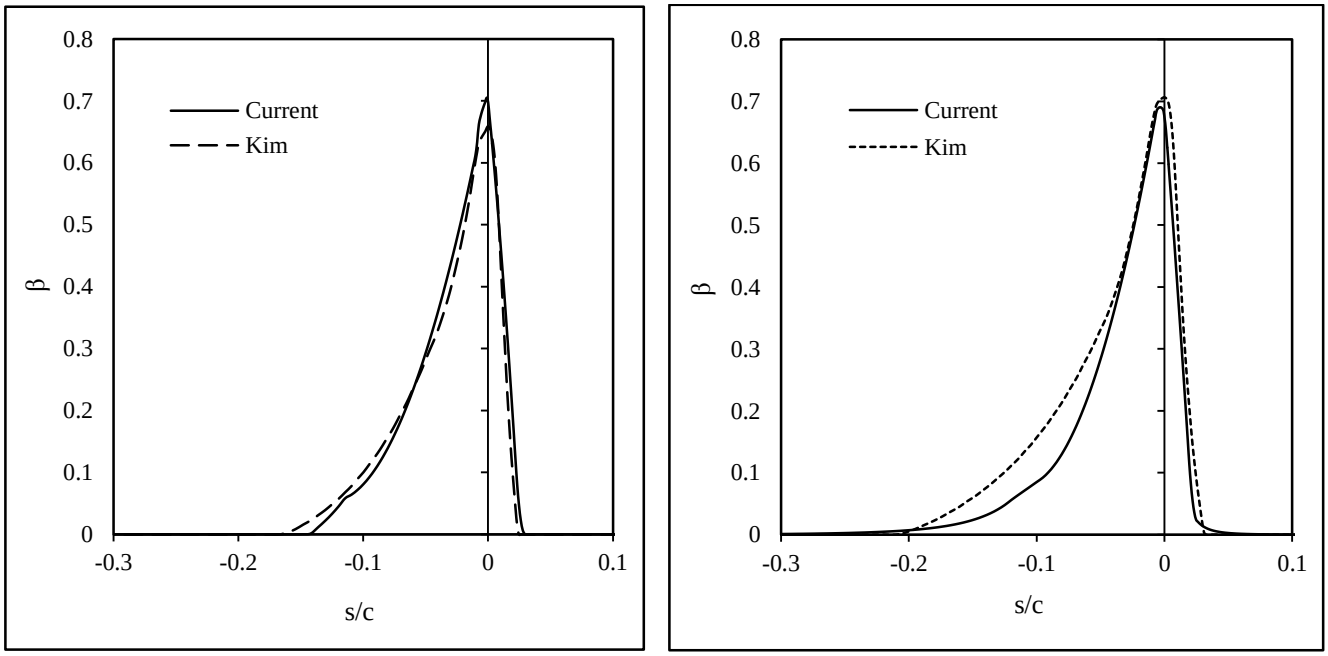

Figure 9: Collections efficiency validation.

(a) MVD = 20 µm, c = 0.53 m, α = 4.0°, V_∞ = 58.10 m/s
(b) MVD = 20 µm, c = 0.53 m, α = 3.5°, V_∞ = 102.8 m/s

Parametric Analysis

The collection efficiency is a function of the free stream velocity, the median volume diameter, the size of the body and the angle of attack. The variation is shown the following figures.

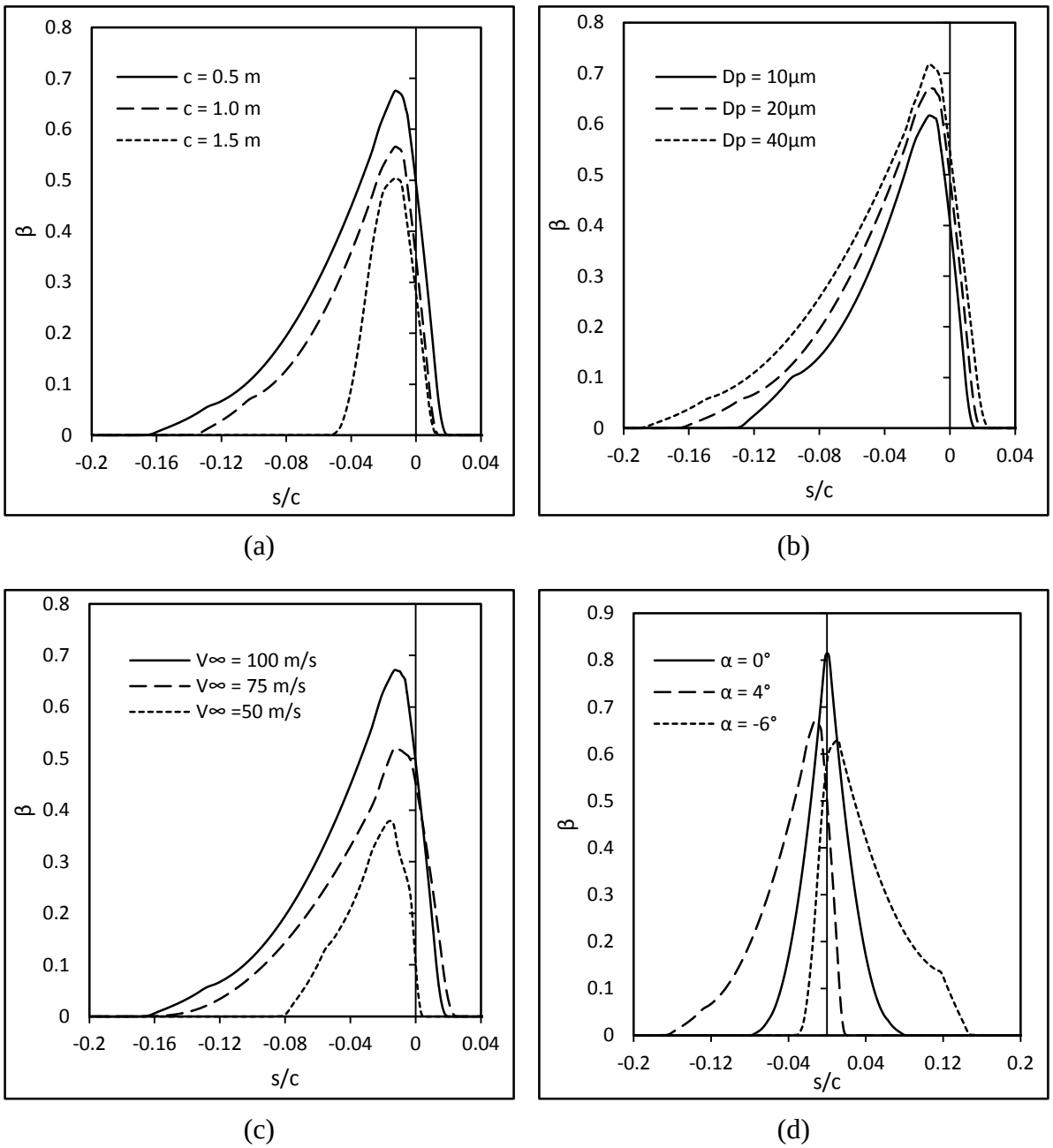

Figure 10: Collections efficiency variations with respect to ambient conditions.

(a) MVD = 20 μm, α = 4.0°, V_∞ = 50 m/s **(b) c = 1.0 m, V_∞ = 50 m/s, α = 4.0°**
(c) MVD = 20 μm, α = 4.0°, c = 1.0 m **(d) c = 1.0 m, V_∞ = 50 m/s, MVD = 20 μm**

The data shown in Figure 10 can be summarized and explained as,

(a) The collection efficiency decreases with the increase in the chord length. This is because larger bodies tend to create more disturbance in the flow and hence the water droplets are dispersed widely and they miss the body with higher frequency.
(b) Larger the diameter of the droplet, higher will be their kinetic energy and hence it will be difficult to change the path of the particles. This increases the probability of hitting the body present in the flow. Therefore, the collection efficiency is higher for the larger droplet diameter than that for smaller droplet diameters.
(c) Similar to the effect of droplet diameter, the velocity of the droplets also determine their kinetic. Greater velocity would mean higher kinetic energy and hence more difficult to divert the droplets and vice versa. As a result, the collection efficiency is higher for high velocities as compared to lower velocities.
(d) The effect of varying angle of attack is similar that of variation in the chord length, for the very same reasons. At an angle of attack of higher magnitude, whether positive or negative, the disturbance in the flow is significant, and hence increases the probability for the droplets to miss the body and travel around it. Thus, increase in angle of attack will always result in a low collection efficiency.
(e) The collection efficiency can be seen as a probability distribution function over the surface of the airfoil with a peak value at the stagnation point and a spread on both the lower and upper surface. The peak value is dependent on all the four parameters and the spread is strictly function of the angle of attack. Changing all the parameters except the angle of attack would cause the curve to shrink or expand only. Changing the angle of attack will result is not only shrinking or expansion of the curve but it also shifts the peak value. The shift is the peak value is in correlation with the shift in the stagnation point.

CHAPTER 6

HEAT TRANSFER COEFFICIENT CALCULATIONS

Transition Prediction

Surface heat transfer rate is calculated for both laminar and turbulent regions separately. Transition is based on roughness height.

$$Re_k = \frac{\rho U_k k_s}{\mu}$$

$$\frac{U_k}{U_e} = 2\frac{k_s}{\delta} - 2\left(\frac{k_s}{\delta}\right)^3 + \left(\frac{k_s}{\delta}\right)^4 + \frac{1}{6}\frac{\delta^2}{\nu}\frac{dU_e}{ds}\frac{k_s}{\delta}\left(1 - \frac{k_s}{\delta}\right)^3$$

$$k_s = \left(\frac{4\sigma_w \mu_w}{\rho_w F \tau}\right)^{\frac{1}{3}}$$

$$\tau = \rho U_e^2 \frac{C_f}{2}$$

δ is the boundary layer thickness computed by Thwaite's method and ds is the distance along the airfoil surface. $Re_k = 600$ is the transition location, as of von Doenhoff [9]. Other necessary parameters are evaluated by well-known empirical relations. Viscosity of air is computed from Sutherland's Law.

Sutherland's Law

$$\mu = \mu_0 \left(\frac{T_0}{T}\right)^{3/2} \frac{T_0 + S}{T + S}$$

$$\mu_0 = 18.27 \times 10^{-6}$$

$$T_0 = 291.15$$

$$S = 120$$

Thwaites' Method

$$\frac{\theta_l^2}{\nu} = \frac{0.45}{U_e^6}\int_0^s U_e^5\, ds$$

$$\delta = \frac{315}{37}\theta_l$$

Laminar Heat Transfer Coefficient

$$h_c = \frac{0.296 k U_e^{1.87}}{\sqrt{\nu \int_0^s U_e^{1.87}\, ds}}$$

Turbulent Heat Transfer Coefficient

The heat transfer rate coefficient in the laminar region is based on Smith and Spalding correlation [9]. In turbulent flows, the method of Kays and Crawford [9] is employed for computing the heat transfer rate.

$$\theta_t = \frac{0.036\nu^{0.2}}{U_e^{3.29}}\left(\int_{s_{tr}}^s U_e^{3.86}\, ds\right)^{0.8} + \theta_{tr}$$

$$\frac{C_f}{2} = \frac{0.1681}{\left[\ln\left(\frac{864\theta_t}{k_s} + 2.568\right)\right]^2}$$

Use Pr=0.72 and Pr_t=0.9,

$$St_k = 1.92 Re_k^{-0.45} Pr^{-0.8}$$

$$St = \frac{\frac{C_f}{2}}{Pr_t + \sqrt{\frac{C_f}{2}\frac{1}{St_k}}}$$

$$h_c = St \rho U_e C_p$$

CHAPTER 7

HEAT AND MASS BALANCE

The thermodynamic model, based on the heat and mass transfer equations derived by Messinger, is used to determine the quantity of ice accreted on each panel of the airfoil. The thickness at which glaze ice first appears needs to be determined.

Extended Messinger Model

Assumptions

1. Ice is in perfect contact with the airfoil surface, which is taken to be at the same temperature as the ambient temperature.
2. The temperature is continuous at the ice water interface and equal to the freezing temperature.
3. At the ice water or ice air interface, heat flux is determined by convection, radiation, latent heat release, cooling by incoming droplets, heat brought in by the runback water, evaporation or sublimation, aerodynamic heating, and kinetic energy of the droplet. These terms are estimated as explained later.

Glaze ice: $$-k_w \frac{\partial \theta}{\partial y} = (Q_c + Q_e + Q_d + Q_r) - (Q_a + Q_k + Q_{in})$$

Rime ice: $$-k_w \frac{\partial T}{\partial y} = (Q_c + Q_s + Q_d + Q_r) - (Q_a + Q_k + Q_{in} + Q_l)$$

4. The surface is initially clean, neither water nor any ice.

$$at \qquad t = 0, \qquad B = h = 0$$

Heat Terms

With the convective heat transfer coefficient h_c , the convective heat transfer Q_c from the surface of water at a temperature T_{sur} to the surrounding at temperature T_a is given by

$$Q_c = h_c(T_{sur} - T_a)$$

Since the incoming droplets are super-cooled, some of the heat is utilized to warm them. This amount of heat is estimated as,

$$Q_d = LWC\ \beta V_\infty C_{pw}(T_{sur} - T_a)$$

Loss of heat through the processes of evaporation Q_e and sublimation Q_s is given by the relations,

$$Q_e = \chi_e e_0 (T_{sur} - T_a) \quad \text{and} \quad Q_s = \chi_s e_0 (T_{sur} - T_a)$$

where $e_0 = 27.03$ $\chi_e = \frac{0.622 h_c L_E}{C_p P_t L e^{2/3}}$ $\chi_s = \frac{0.622 h_c L_S}{C_p P_t L e^{2/3}}$

The radiation heat loss Q_r is estimated as,

$$Q_r = 4\varepsilon\sigma_r T_a^3 (T_{sur} - T_a)$$

The aerodynamic heating Q_a is given by,

$$Q_a = \frac{r h_c V_\infty^2}{2C_p}$$

The kinetic energy of the droplets can calculated from,

$$Q_k = (\beta V_\infty G)\frac{V_\infty^2}{2}$$

Finally, the energy brought in by the runback water is given as,

$$Q_{in} = \dot{m}_{in} C_{pw} (T_f - T_{sur})$$

Ice Thickness

Rime ice thickness is given by,

$$B = \left(\frac{\beta V_\infty G + \dot{m}_{in} - \dot{m}_s}{\rho_r}\right) t$$

The temperature distribution in the rime ice layer is observed to be governed by [9],

$$\frac{\partial^2 T}{\partial y^2} = 0$$

Twice integrating this equation and using the boundary conditions, we get

$$T(y) = T_s + \frac{(Q_a + Q_k + Q_{in} + Q_l) - (Q_c + Q_s + Q_d + Q_r)}{k_i} y$$

or

$$T(y) = T_s + \frac{Qr_0 + Qr_1 T_s}{k_i - Qr_1 B}\, y$$

where,

$$Qr_0 = \rho_r L_F \frac{\partial B}{\partial t} + \beta V_\infty G \frac{V_\infty^2}{2} + \frac{r h_c V_\infty^2}{2C_p} + \beta V_\infty G C_{pw} T_a + h_c T_a + 4\varepsilon\sigma_r T_a^4 + \chi_s e_0 T_a + \dot{m}_{in} C_{pw} T_f$$

$$Qr_1 = \beta V_\infty G C_{pw} + h_c + 4\varepsilon\sigma_r T_a^3 + \chi_s e_0 + \dot{m}_{in} C_{pw}$$

In case of the glaze ice, the following equations hold,

$$\frac{\partial^2 T}{\partial y^2} = 0$$

$$\frac{\partial^2 \theta}{\partial y^2} = 0$$

which yeilds,

$$T(y) = T_s + \frac{T_f - T_s}{B} y$$

and

$$\theta(y) = T_f + \frac{(Q_a + Q_k + Q_{in}) - (Q_c + Q_s + Q_d + Q_r)}{k_i}(y - B)$$

or

$$\theta(y) = T_f + \frac{Q_0 + Q_1 T_f}{k_w - Q_1 h}\, y$$

where Q1 and Q0 are functions of ambient conditions given by,

$$Q_0 = \rho_a \beta V_\infty \frac{V_\infty^2}{2} + r h_c \frac{V_\infty^2}{2\, C_{pa}} + \rho_a\, \beta\, V_\infty C_{pw}\, T_a + h_c T_a + 4\epsilon\sigma_r T_a^4 + \chi_e\, e_0\, T_a \;+\; \dot{m}_{in} C_{pw}\, T_f$$

$$Q_1 = \rho_a \beta V_\infty C_{pw} + h_c + 4\epsilon\sigma_r T_\infty^3 + \chi_e\, e_0 \;+\; \dot{m}_{in} C_{pw}$$

and the height of the water h is given by,

$$h = \left(\frac{\rho_a \beta V_\infty + \dot{m}_{in} - \dot{m}_{sub}}{\rho_w}\right)(t - t_g) - \frac{\rho_g}{\rho_w}(B - B_g)$$

the rate of glaze ice growth is given by the ordinary 1st order differential equation,

$$\rho_g L_F \frac{\partial B}{\partial t} = k_i \frac{T_f - T_s}{B} - k_w \frac{Q_0 + Q_1 T_f}{k_w - Q_1 h}$$

The formation of glaze or rime ice is based on the parameters B_g and t_g, which are defined as

$$B_g = \frac{k_i(T_f - T_s)}{\rho_g L_F \left(\frac{\rho_a \beta V_\infty + \dot{m}_{in} - \dot{m}_{sub}}{\rho_r}\right) + (Q_0 + Q_1 T_f)}$$

$$t_g = \left(\frac{\rho_r}{\rho_a \beta V_\infty + \dot{m}_{in} - \dot{m}_{sub}}\right) B_g$$

The above equations give a quantitative measure for the type of ice formed. Only rime ice forms when $B_g \leq 0$ and $t_g > t_{exp}$. In this case, the thickness of ice and the freezing fraction are given by

$$B = \left(\frac{\rho_a \beta V_\infty + \dot{m}_{in} - \dot{m}_{sub}}{\rho_r}\right) t$$

$$FF = \frac{\rho_r B}{(\rho_a \beta V_\infty + \dot{m}_{in}) t}$$

Glaze ice forms when $B_g > 0$ and $t_g \leq t_{exp}$. Glaze ice is calculated by solving the following differential equation using Runge-Kutta-Fulhberg method.

$$\rho_g L_F \frac{\partial B}{\partial t} = k_i \frac{T_f - T_s}{B} - k_w \frac{Q_0 - Q_1 T_f}{k_w - Q_1 h}$$

In this case, we get freezing fraction by

$$FF = \frac{\rho_r B_g + \rho_g (B - B_g)}{(\rho_a \beta V_\infty + \dot{m}_{in}) t}$$

Runback water mass flow rate is given by

$$\dot{m}_{out} = (1 - FF)(\rho_a \beta V_\infty + \dot{m}_{in}) - \dot{m}_e$$

CHAPTER 8

VALIDATION

Validation is a process of establishing the worthiness or legitimacy of a tool or instrument. In the engineering world, it follows a path of comparing the results to the physical reality for consistency. Thus it is obligatory for every new tool to undergo this process to establish its worthiness and legitimacy.

Validation Cases

In flight icing on both aircrafts and rotorcrafts have been extensively studied as compared to icing on wind turbines. Hence, there is sufficient aircraft icing data available for comparison and validation. These data include data from wind tunnel experiments as well as numerical codes like LEWICE, TURBICE, FENSAP, etc. Reference [10] contains ice shapes for several icing cases. The following cases were picked for the validation of the current code.

Table 1: Conditions for validation cases.

Parameters	Airfoil	c	α	V_∞	T_∞	P_∞	LWC	MVD	T_{exp}
Units	--	m	°	m/s	K	kPa	g/m^3	μm	s
CASE 27	NACA0012	0.53	4.0	58.1	245.2	95.61	1.3	20.0	480
CASE 28	NACA0012	0.53	4.0	58.1	253.2	95.61	1.3	20.0	480
CASE 29	NACA0012	0.53	4.0	58.1	259.1	95.61	1.3	20.0	480
CASE 30	NACA0012	0.53	4.0	58.1	266.3	95.61	1.3	20.0	480
CASE 37	NACA0012	0.152	0.0	130.5	260.7	90.50	0.5	17.5	120
CASE 38	NACA0012	0.152	8.5	130.5	260.7	90.50	0.5	17.5	120

There is a range of ambient conditions for the validation cases for the same geometry. The most varying parameter is the temperature whereas there are two instants for the other parameters. The validation cases include conditions both for glaze and rime ice. Case 27 is a pure rime ice case where as glaze ice is expected to form for the Case 30.

The icing simulation is a multistep process with more number of steps being considered more accurate which comes at the cost of computational resources. So, it's necessary to find a compromise between accuracy and computational cost. It has been observed that for the icing simulations, 4 time steps gives reasonable results. Hence, four time steps are used for the validation cases.

The results of a four time steps simulation for cases given in Table 1 are shown in figures Figure 11 to Figure 16. The results are compare with experimental data and data from LEWICE [10].

The results are acceptable within numerical inaccuracies. The ice shapes are not perfectly in agreement with the experimental results because of the inherent shortcomings of the model as well as numerical inaccuracies. The disagreement is more vividly apparent in the glaze ice case.

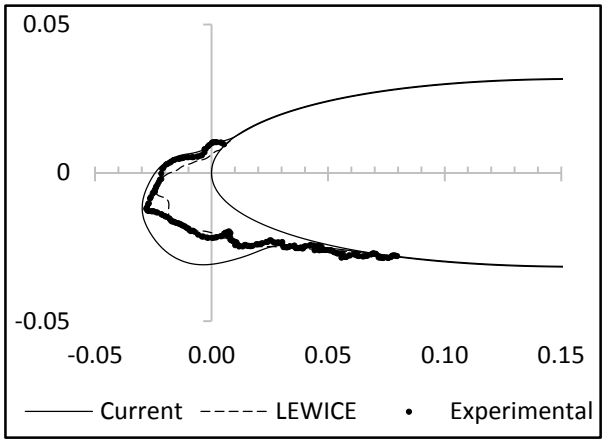

Figure 11: Ice shape Case 27

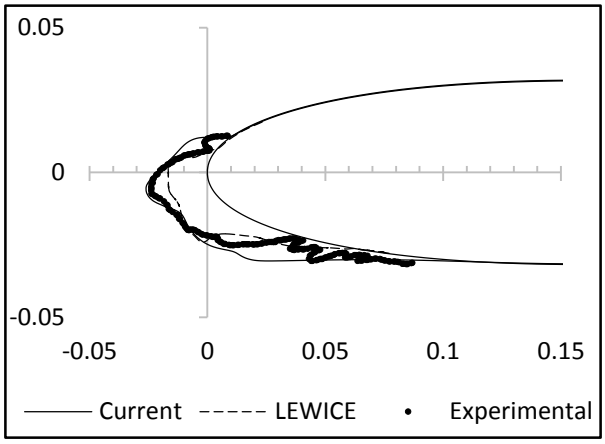

Figure 12: Ice shape Case 28

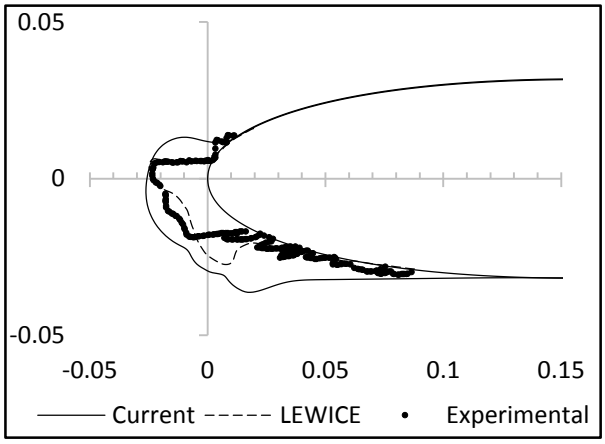

Figure 13: Ice shape for Case 29

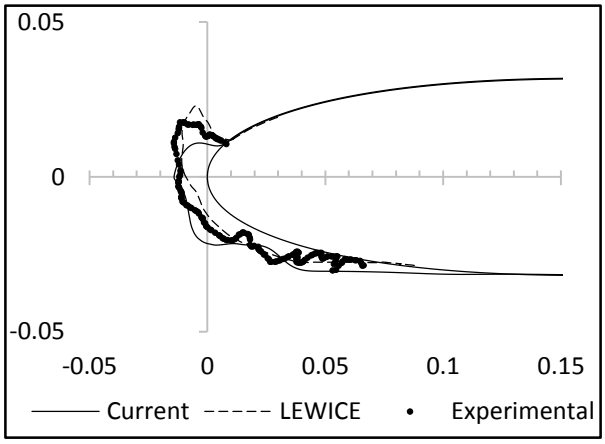

Figure 14: Ice shape for Case 30

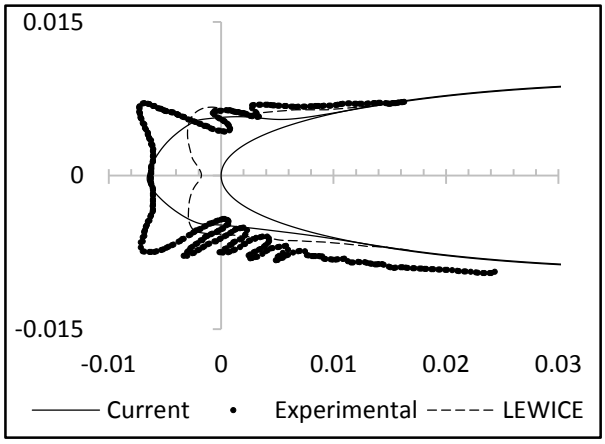

Figure 15: Ice shape for Case 37

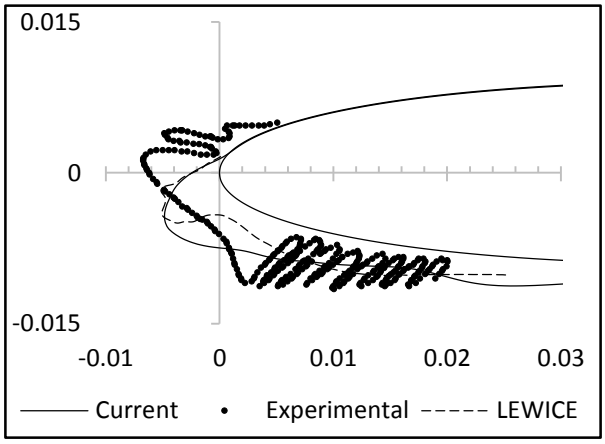

Figure 16: Ice shape for Case 38

CHAPTER 9

CASE STUDIES

As a test case, an experimental wind turbine was studied for a set of ambient conditions. The turbine under investigation is a two tapered and twisted blades designed for the Combined Rotor Experiment (CER) of the National Renewable Energy Laboratory. The turbine is designed for a rated power of 20 KW.

Blade Geometry

The blade uses an S809 airfoil nonlinear twist and linear .taper. The radial twist and chord distributions are given in the following figures. The 2-bladed wind turbine rotated at a constant speed of 72 RPM and used a linearly tapered, non-linearly twisted S809 airfoil geometry with a 3 degree pitch and a stall regulated motor. The turbine's radius from the center of rotation was 5.03 m which includes both the blade and the hub.

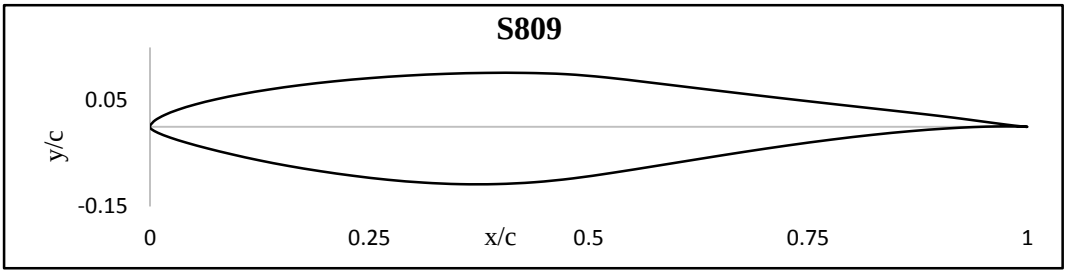

(a) S809 airfoil shape.

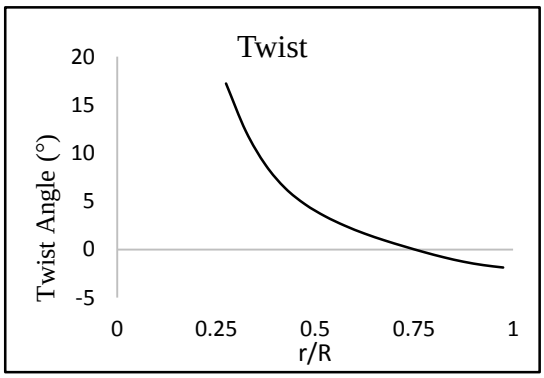

(b) Non-linear twist.

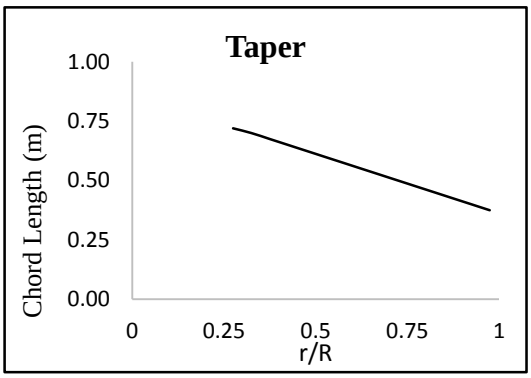

(c) Linear taper.

Figure 17: The geometry of the blade.

Airfoil Characteristics

The S809 airfoil is a specialized airfoil designed specifically for wind turbine applications. The drag polar is given below.

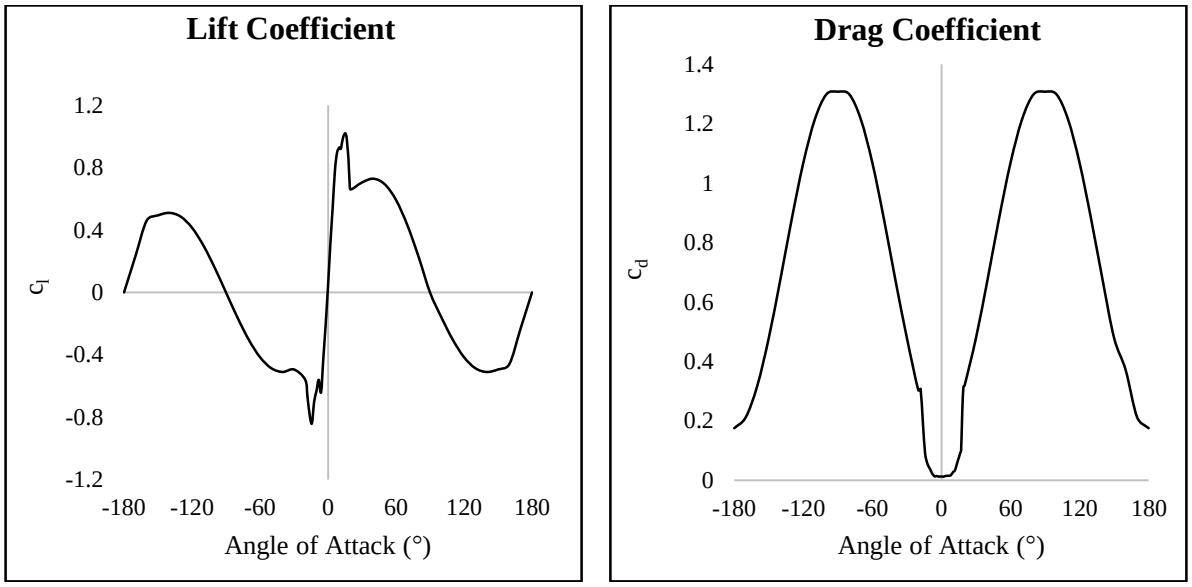

Figure 18: S809 airfoil characteristics.

Turbine Performance Predictions

The turbine gives the required power at a rotor speed of 72 RPM. The power curves at different pitch settings are given if the figure below.

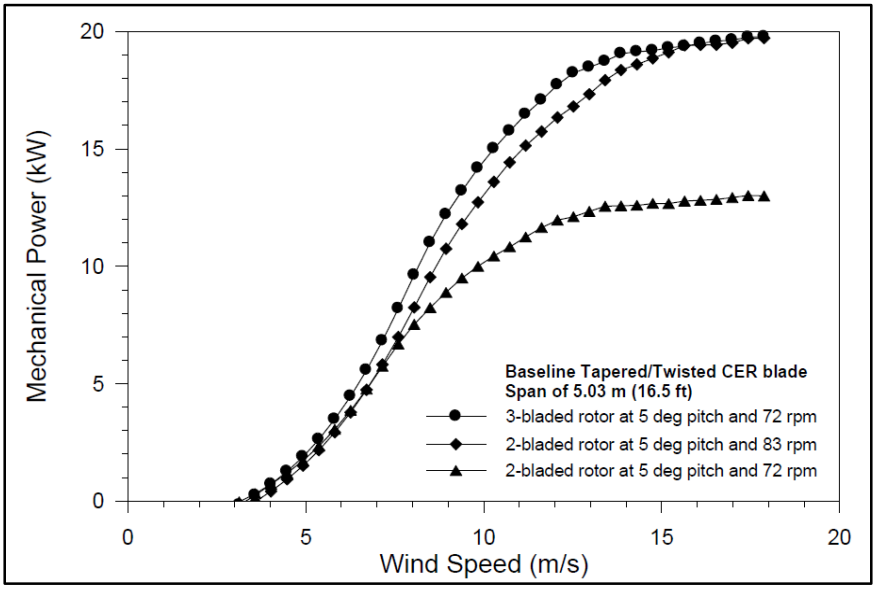

Figure 19: Power curves.

Radial Sections

The blade element theory divides the blade into radial sections. The accuracy is improved by using a greater number of sections. It has been observed that more than 15 sections do not improve the results. Hence a total number of 15 sections were analyzed for the current study. As shown below, the sections are numbered 1-15 starting from the hub till the tip.

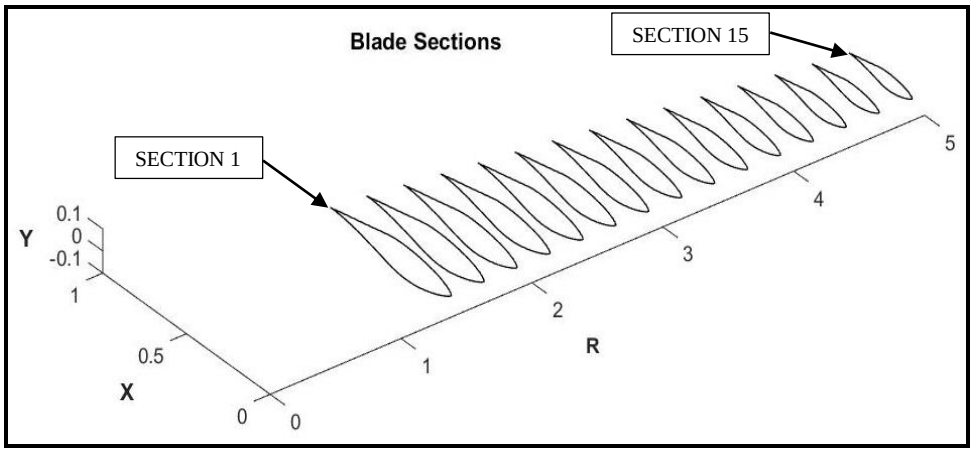

Figure 20: Blade radial sections.

Test conditions

Three cases were run for which the conditions are given below.

Table 2: Conditions for cases studies

Parameters	φ	RPM	V_∞	T_∞	P_∞	LWC	MVD	T_{exp}
Units	°	RPM	m/s	K	kPa	g/m3	µm	s
CASE I	3.0	72	10	270.4	101325	0.22	20	1800
CASE II	2.0	72	10	270.4	101325	0.22	20	1800
CASE III	6.0	72	10	270.4	101325	0.22	20	1800

Radial Distribution of Collection Efficiency

As discussed in the previous chapter, the collection efficiency is a function of the chord length, angle of attack, free stream velocity and the droplet median volume diameter. Except for the MVD, all the other three parameters vary along the radius of the blade. Thus each section will have a different collection efficiency depending on their radial location. Because of the taper, the chord decreases, as do the angle of attack. Results indicate that mostly outboard of a turbine blade is most prone to icing.

The figure below, the x-axis is the radial locations and y-axis is the length along the chord non-dimensionalized by the chord starting from the leading edge with the lower surface as negative. The z-axis gives the collection efficiency.

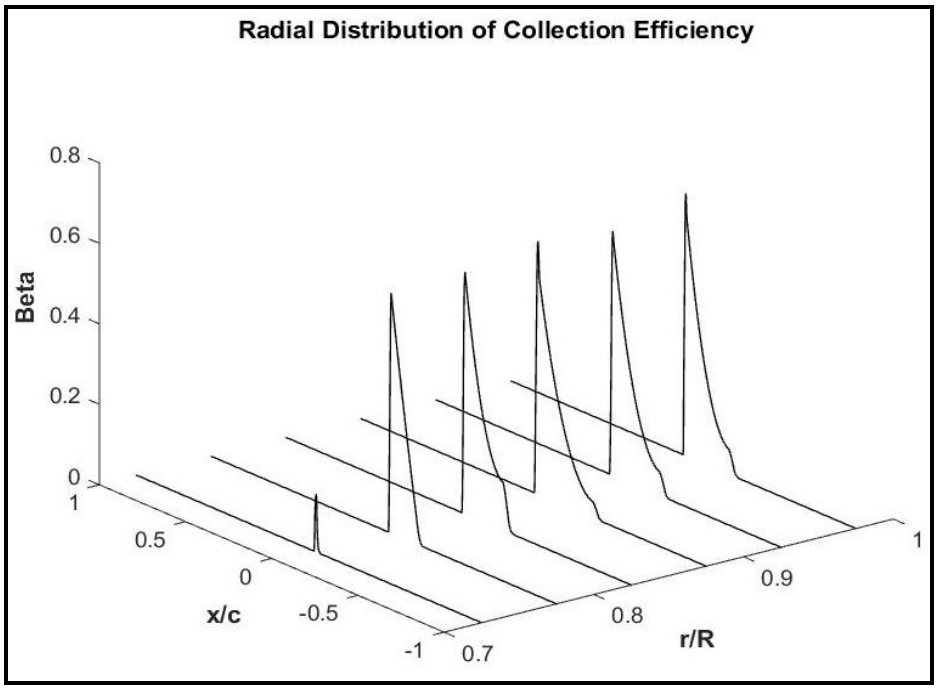

Figure 21: Distribution of collection along the radius.

Case I

For case I, only two outboard sections gets ice. The rest of blade has no droplet impingement at all. Because of the taper and the twist, the in board sections have high local effective angle of attack and have larger chord. This forces the water droplets to dodge around the section rather than hitting it. The droplet collection distribution over the clean airfoil for case I is shown in Figure 22. The resulting ice shapes suggest that the distribution changes for the subsequent layers.

Collection Efficiency

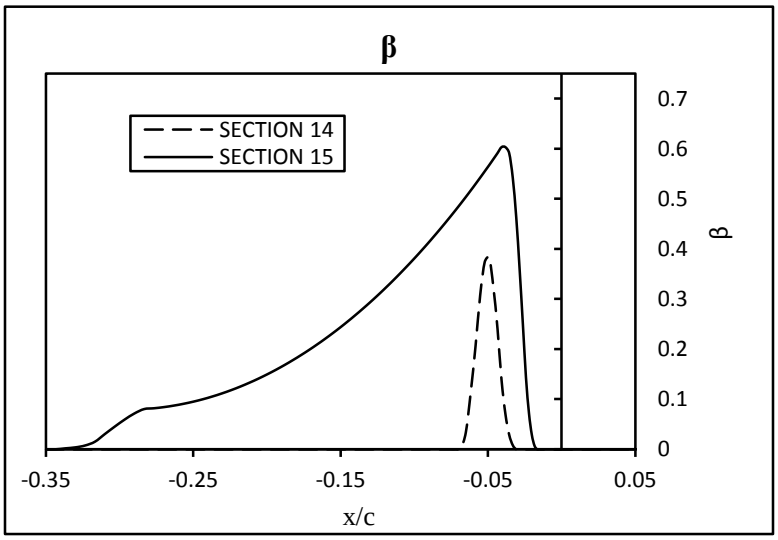

Figure 22: Collection efficiency for Case I.

Ice Shapes

The resulting ice shapes for the two section are shown in Figure 23. Section at 92.5 % radius has only a bubble on the lower surface whereas section at 97.5 % radius has a layer of ice on the bottom surface towards the leading edge.

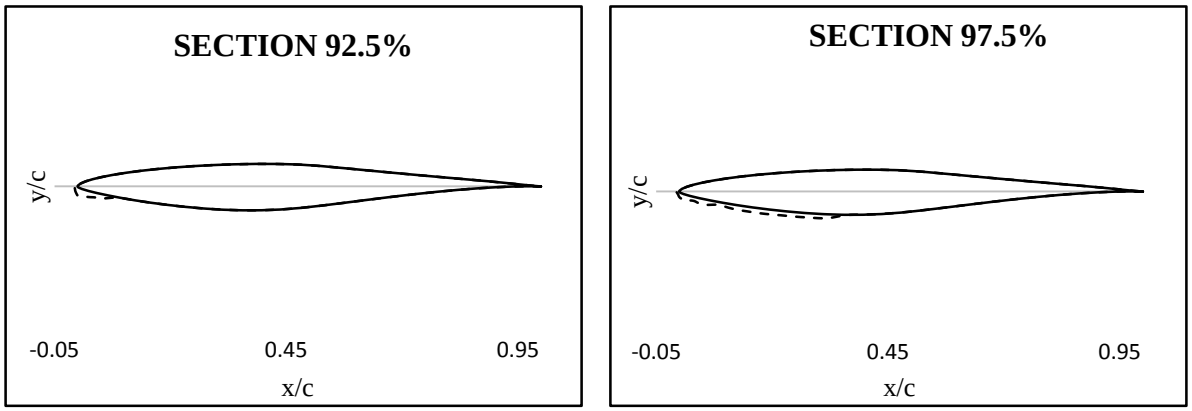

Figure 23: Ice shapes for sections at 92.5 and 97.5 percent radius.

Power Loss

For both the sections, the leading edge is affected which alters the flow over the airfoil especially on the upper surface, if the airfoil is operating at a positive angle of attack. As a result, the airfoil characteristic is dramatically changed. The effect can be seen in the power curve in Figure 24 for a given pitch angle and wind velocity. The power loss is very significant for the outboard iced sections revealing loss of lift and increased in drag for these sections. The loss of lift may be attributed to the early separation because of the leading edge ice. The increase in drag is a result of both separation on the upper surface and increased skin friction on the lower surface. The roughness of the ice layer causes the skin friction to rise.

Figure 25 shows the power curve for both clean blade and the iced blade at a pitch angle of 3°. The power loss is significant at and near the design wind speed of 10 m/s.

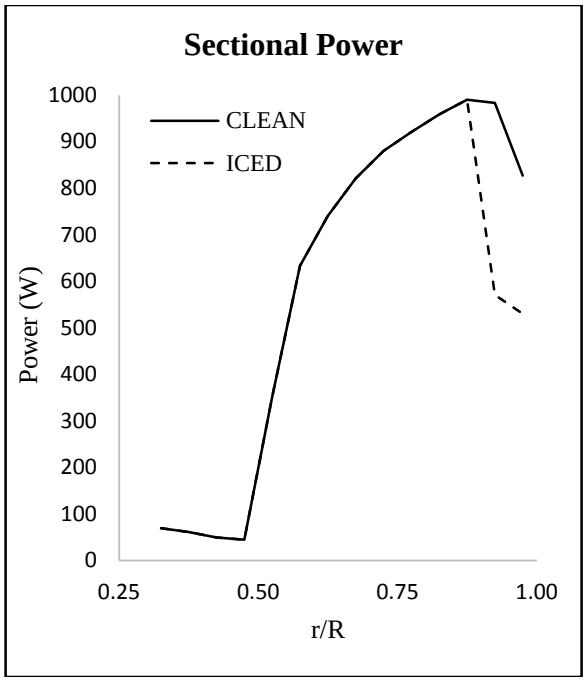

Figure 24: Sectional power loss at 10 m/s wind velocity and 3° pitch angle.

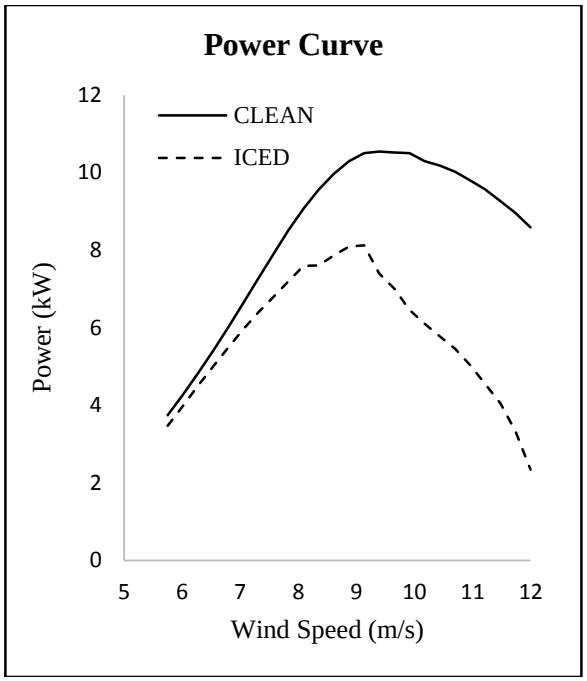

Figure 25: Power curve for Case I at 3°pitch angle.

Case II

Similar to case I, for case II only two outboard sections gets ice. The rest of blade has no droplet impingement at all.

Collection Efficiency

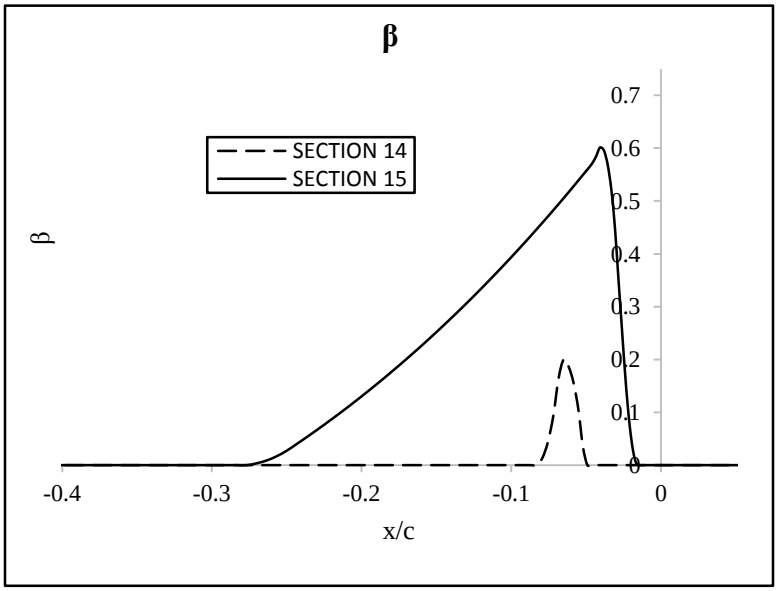

Figure 26: Collection efficiency for Case II.

Ice Shapes

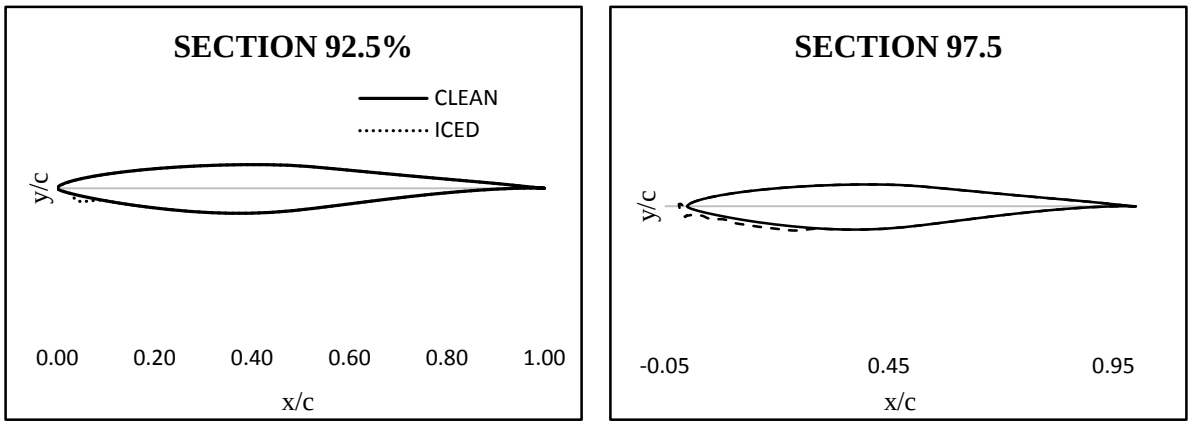

Figure 27: Ice shapes for sections at 92.5 and 97.5 percent radius.

Power Loss

Section at 92.5 % radius seems to be insensitive to the ice formed as the power loss is not notable. This is because the ice is not right at the leading edge. Being on the lower surface aft the leading edge, the ice layer is ineffective in disturbing the flow on the upper surface. Moreover, it is concentrated in a small locality, hence the contribution towards skin friction is negligible as well. Unfortunately, for section at 97.5 % radius, not only the ice is formed on right on the leading edge, but also it covers a reasonable surface on the lower surface, hence responsible for both flow separation and making the surface coarse.

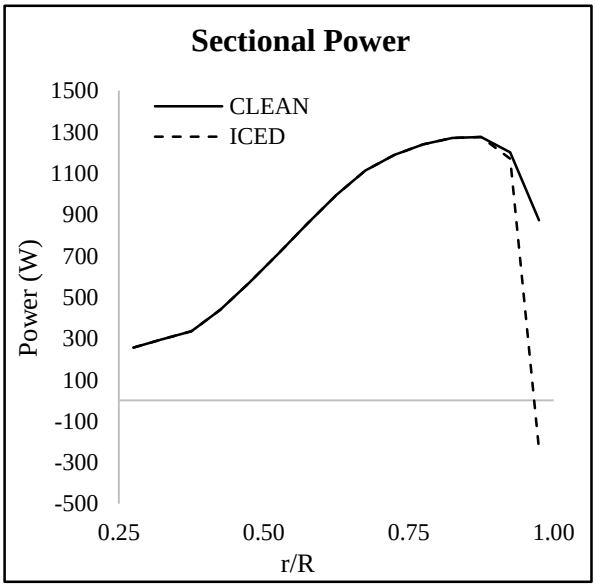

Figure 28: Sectional power at 10 m/s wind velocity and 3° pitch angle.

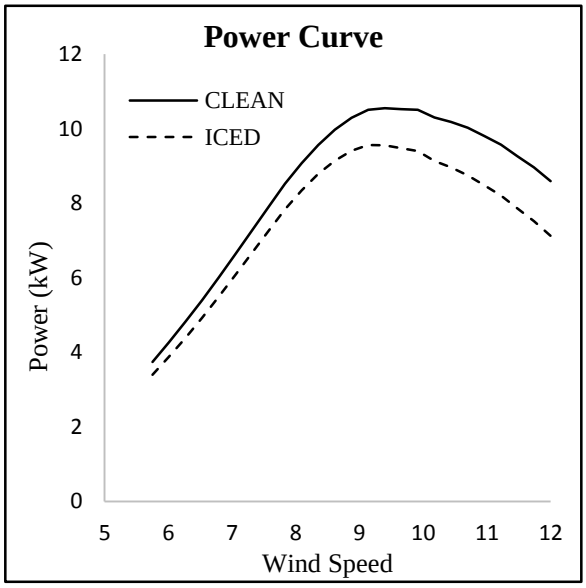

Figure 29: Power curve for Case II at 3° pitch angle.

Case III

For case III, five outboard sections get the ice. Rest of the inboard sections do not collect any water droplet. The collection efficiency is distributed similar to the previous cases with the bottom surface getting a lot of it.

Collection Efficiency

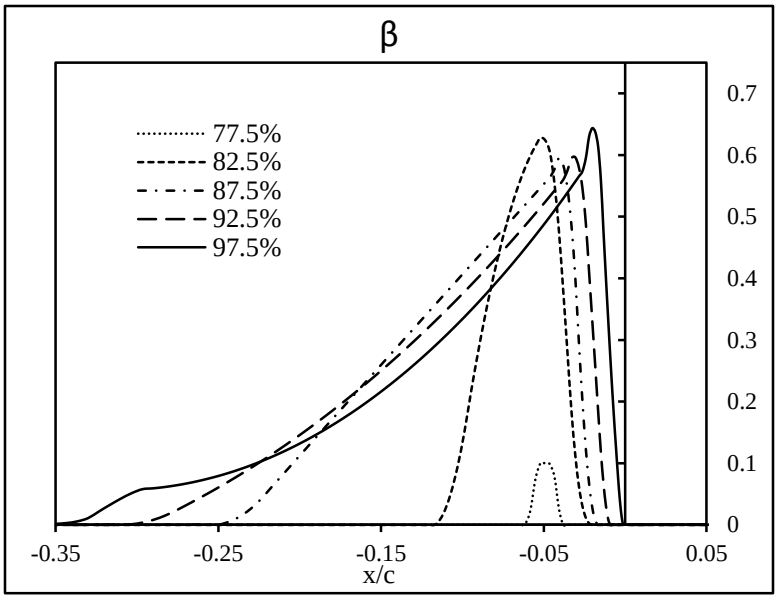

Figure 30: Sectional collection efficiency at 10 m/s wind velocity and 3° pitch angle.

For section at 77.5 % radius, there is a little droplet catchment and hence a concentrated mass of ice on the bottom surface, as shown is the Figure 31. The resulting aerodynamic characteristics are not very different form the clean airfoil, hence not presented here. For the rest of the sections, there is total loss of lift for many angle of attacks.

Ice Shapes

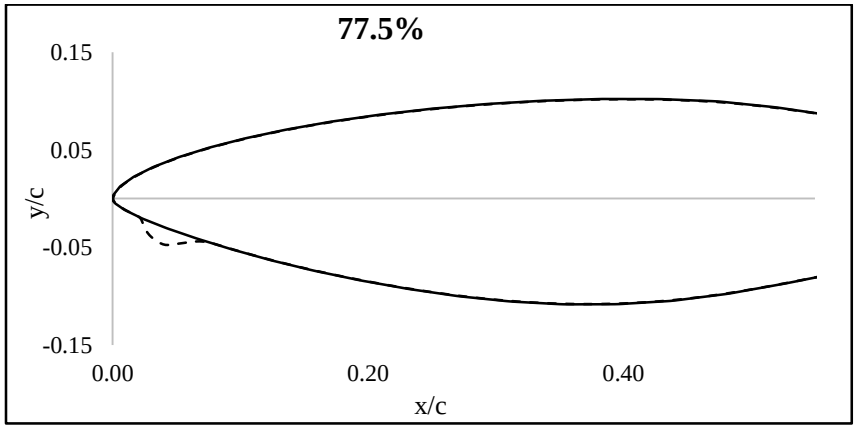

Figure 31: Ice shapes for section 77.5 percent radius.

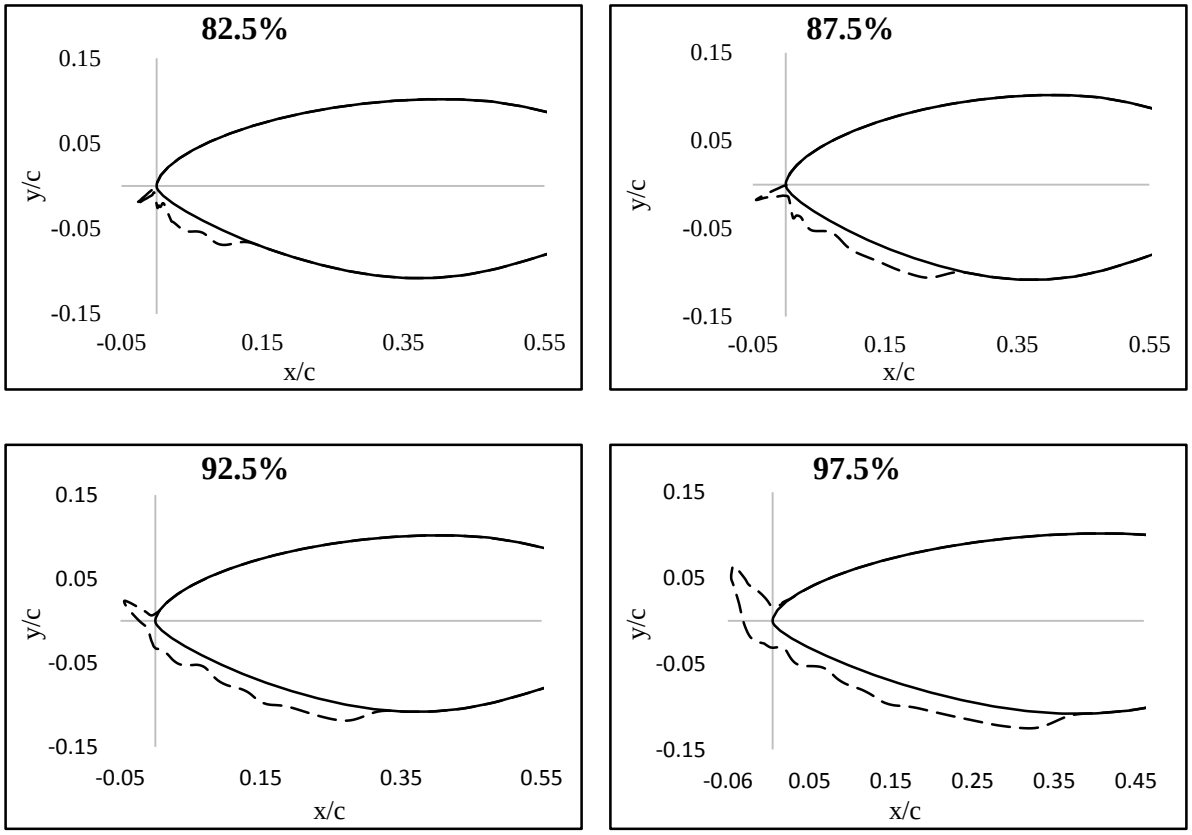

Figure 32: Ice shapes for sections at 82.5, 87.5, 92.5 and 97.5 percent radius.

Power Loss

Before looking at the performance of the blade, let us look at the aerodynamic characteristics of the iced sections in more details. Figure 33 and Figure 34 give the lift and drag curves for the iced sections in comparison with the clean airfoil.

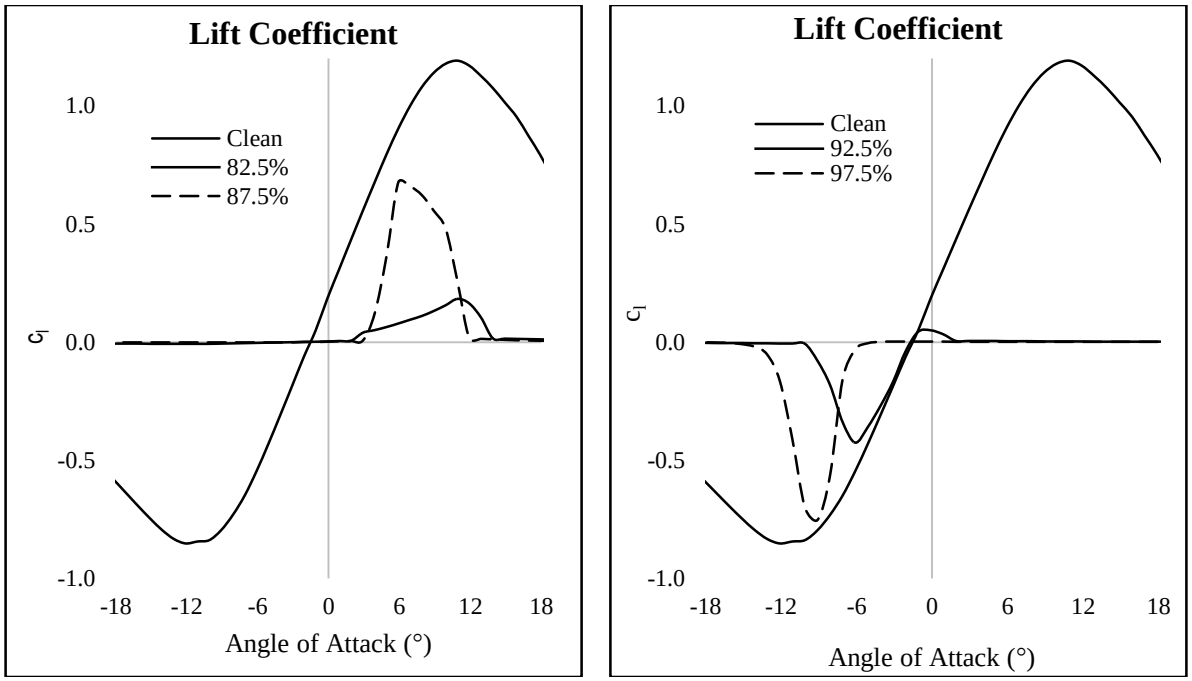

Figure 33: Lift curve for sections at 82.5, 87.5, 92.5 and 97.5 percent radius.

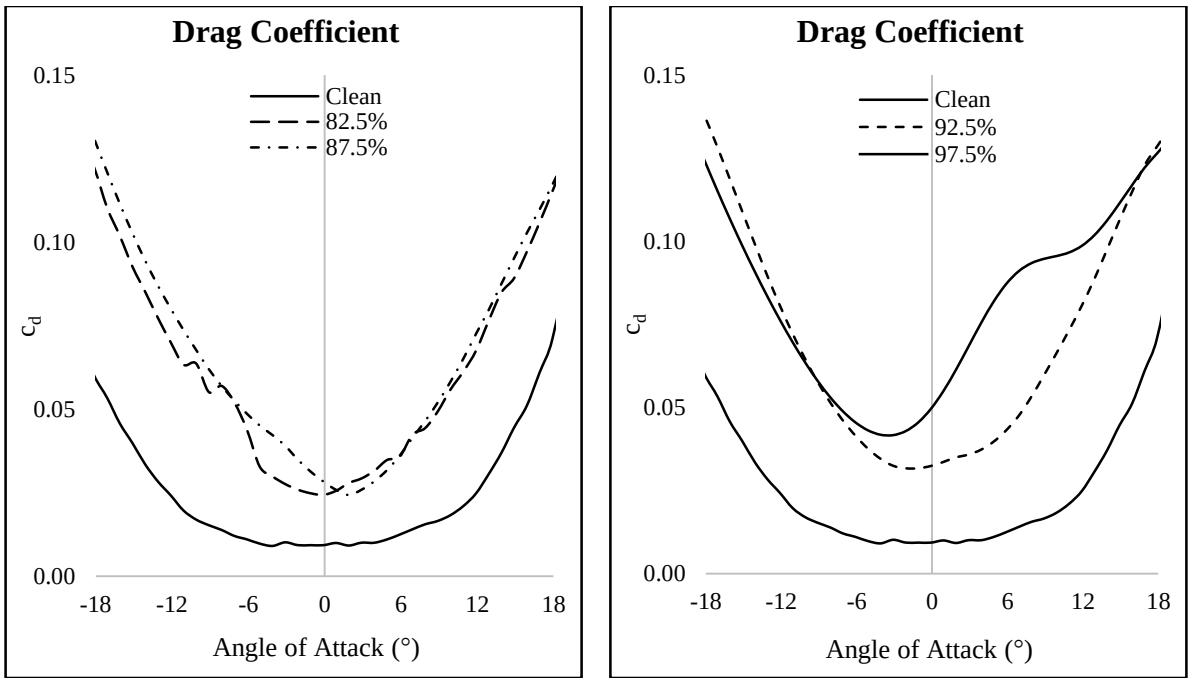

Figure 34: Drag curve for sections at 82.5, 87.5, 92.5 and 97.5 percent radius.

Dramatic loss in lift can be seen for the four sections because of the sharp ice layer at the leading edge. For the sections at 82.5 % and 87.5% radii, the ice is pointing in the lower direction. Such a shape acts like a leading edge flap shifting the lift curve. But unlike the leading edge flaps, the ice shape are permanent structures which cannot be controlled. Hence the usefulness is short-lived and the ice adversely interfere with the flow. For the similar reasons as stated for case II, loss of lift and increase in drag is observed for case II as well.

The performance of the four out board sections is reduced to power consumption rather than producing power. The net effect is around 40% of power loss at the rated operating conditions.

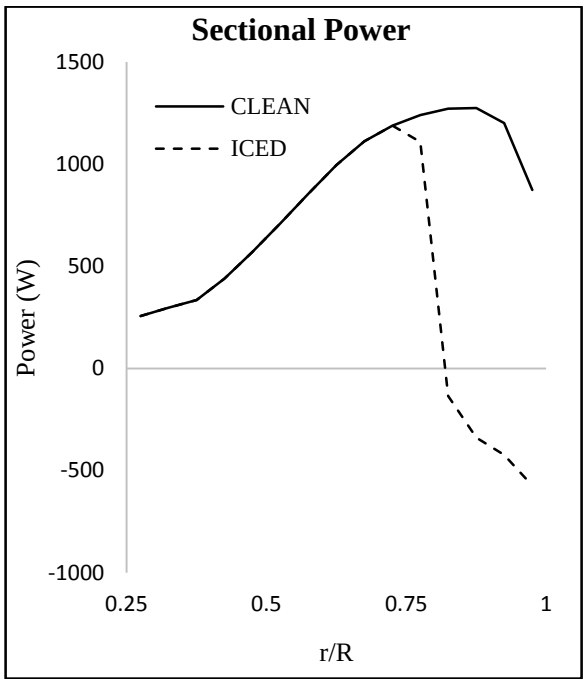

Figure 35: Sectional power loss at 10 m/s wind velocity and 3° pitch angle.

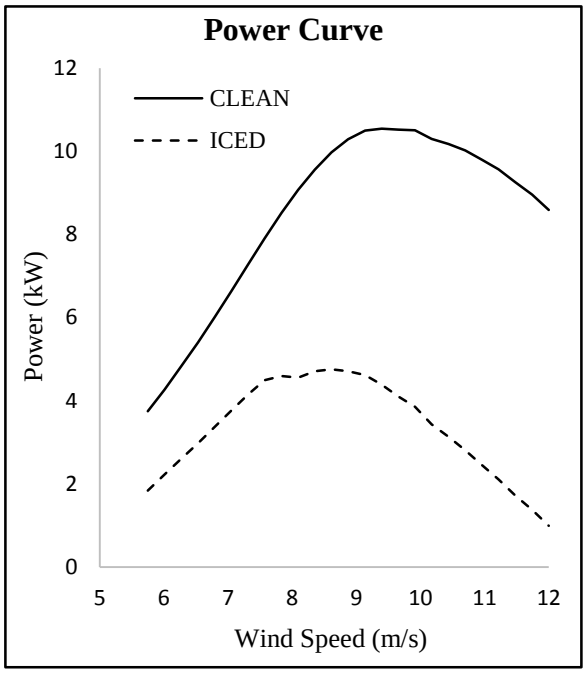

Figure 36: Power curve for Case III at 3° pitch angle.

CHAPTER 10

CONCLUSIONS

The development of a stand-alone and dedicated tool to predict the ice accumulation on wind turbine blades will help in ensuring the continued operation in cold climates. This will enable the wind energy industry to take a priori measures in a cost efficient manner. The inclusion of weather data in the simulation will make the tool high fidelity. So far, the results obtain so far is reasonable enough within numerical inaccuracies which can be improved by using more robust and efficient algorithms.

Computational Cost

As for every computational setup, it is necessary to keep track of the computational time, the computation time for the problem at hand has also been investigated. Table 3 presents the breakdown of the computation time for each module for a typical simulation with 4 layers and 15 sections. The breakdown shows the computation of collection efficiency to be the most expensive one. It is because of the time stepping nature of the problem formulation as the calculations involves marching in time throughout the flow domain.

Table 3: Computational cost breakdown.

Module	Computation Time (s)	Percentage of Total Time
Blade Element Momentum Theory	5.8	0.05%
Panel Method	166	1.40%
Convective Heat Transfer Coefficient	4.3	0.04%
Collection Efficiency	11566	97.65%
Extended Messinger Model	2.28	0.02%
Miscellaneous	100.2	0.85%
Total	**11844.7**	**100%**

Critical Locations

As have discussed earlier, the water droplet collection efficiency is dependent on the chord length, angle of attack and velocity at a given location. These parameters varying along the span of the wind turbine blade. The combination of these parameters for the inboard section are not favorable for the catchment of the droplets. On the contrary, they form a favorable combination on the outboard sections. Thus, the outboard sections of the blade are more sensitive to ice accretion than the inner sections. Also, the contribution of outboard sections is prominent, the loss of power generation at these sections is felt as a heavy penalty.

Iced formed on the leading edge is high detrimental for the power production as it completely changes the flow over the upper surface. So, if somehow the leading edge is protected from ice accumulation, the performance degradation may be reduced.

Sensitivity

For the current study, only variation in pitch angle was considered. The collection efficiency is heavily dependent on the pitch angle and hence the overall ice accumulation. The study shows a power loss of 10% to 40% for different pitch settings. So, it is apparent from this study that controlling the pitch may be very effective way of avoiding the ice accumulation on the turbine blades.

Recommendations

Based on the observations in this study, it is recommended that;

1. The code may further be developed to enable its used for unsteady ambient conditions which will make it possible to predict the performance evaluation of wind turbines operating in cold climates using the weather forecast.

2. The calculation of collection efficiency consumes most of the time, so it is strongly recommended to use alternate methods, if the simulations are run for longer period of time and for higher number of steps.

3. Operating the wind turbines at low pitch angles during the icing climate may reduce the chances of ice accumulation.

4. If anti-icing or de-icing is sought, they should be place outboard and towards the leading edge of the airfoil.

5. The data generated should be used to determine the effects on the structural dynamics of the blades which in turn will predict the fatigue life of the blades.

APPENDIX

Table 4: Values of constants (air and water properties).

Symbol	Description	Value	Units
C_p	Specific heat of air	1006	J/Kg K
C_{pi}	Specific heat of ice	2050	J/Kg K
C_{pw}	Specific heat of water	4218	J/Kg K
e_0	Saturation vapor pressure constant	27.03	--
g	Gravitational acceleration	9.81	m/s^2
k_i	Thermal conductivity of ice	2.18	W/m K
k_w	Thermal conductivity of water	0.571	W/m K
Le	Lewis number	1/Pr	J/Kg
L_F	Latent heat of solidification	3.3440×10^5	J/Kg
L_E	Latent heat of vaporization	2.5000×10^6	J/Kg
L_S	Latent heat of sublimation	2.8344×10^6	J/Kg
Pr	Laminar Prandtl number of air	0.72	--
Pr_t	Turbulent Prandtl number of air	0.9	--
ε	Radiative surface emissivity of ice	0.75	--
μ_w	Viscosity of water	1.795×10^{-3}	Pa s
ρ_r	Density of rime ice	880	Kg/m^3
ρ_g	Density of glaze ice	917	Kg/m^3
ρ_w	Density of water	999	Kg/m^3
σ_r	Stefan-Boltzmann constant	5.6704×10^{-8}	--
σ_w	Surface tension of water	0.072	N/m

REFERENCES

1. Dalili, N., A. Edrisy, and R. Carriveau, *A review of surface engineering issues critical to wind turbine performance.* Renewable and Sustainable Energy Reviews, 2009. **13**(2): p. 428-438.
2. Makkonen, L., *Models for the Growth of Rime, Glaze, Icicles and Wet Snow on Structures*. 2000, The Royal Society. p. 2913.
3. Switchenko, D., et al. *FENSAP-ICE Simulation of Complex Wind Turbine Icing Events, and Comparison to Observed Performance Data*. in *32nd ASME Wind Energy Symposium*. Place of Publication: Reston, VA, USA; National Harbor, MD, USA. Country of Publication: USA.: American Institute of Aeronautics and Astronautics.
4. Gent, R.W., N.P. Dart, and J.T. Cansdale, *Aircraft Icing*. 2000, The Royal Society. p. 2873.
5. Myers, T.G., *Extension to the Messinger Model for Aircraft Icing.* AIAA Journal, 2001. **39**(2): p. 211.
6. Moran, J., *An introduction to theoretical and computational aerodynamics / Jack Moran*. 1984: New York : Wiley, c1984.
7. Houghton, E.L., *Aerodynamics for engineering students*. 5th ed. ed, ed. P.W. Carpenter. 2003, Butterworth-Heinemann: Oxford ;.
8. Kim, J., et al. *Ice Accretion Modeling Using an Eulerian Approach for Droplet Impingement*. 2013. Red Hook NY, Curran Associates.
9. Ozgan, S., Cambek, M., *Ice accretion simulation on multi-element airfoils using extended Messinger model.* Heat & Mass Transfer, 2009. **45**(3): p. 305-322.
10. Wright, W.B., R.W. Gent, and D. Guffond, *DRA/NASA/ONERA collaboration on icing research. Part II, Prediction of airfoil ice accretion [microform] / William B. Wright, R.W. Gent, Didier Guffond*. NASA contractor report: 202349. 1997: [Washington, DC : National Aeronautics and Space Administration ; Springfield, Va. : National Technical Information Service, distributor, 1997].